

# **Ferroelastic Twin Domains in Methylammonium Lead Iodide Perovskites**

von

**Leonard Elias Winkelmann**

Masterarbeit in Physik  
vorgelegt dem Fachbereich Physik, Mathematik und Informatik (FB 08)  
der Johannes Gutenberg-Universität Mainz  
am 16. August 2019

1. Gutachter: Prof. Dr. Stefan Weber
2. Gutachter: Prof. Dr. Hans-Joachim Elmers

Ich versichere, dass ich die Arbeit selbstständig verfasst und keine anderen als die angegebenen Quellen und Hilfsmittel benutzt sowie Zitate kenntlich gemacht habe.

Mainz, den 16. August 2019

Leonard Elias Winkelmann  
AK Weber  
Max-Planck-Institut für Polymerforschung  
Ackermannweg 10  
D-55128 Mainz  
[Winkelmann@mpip-mainz.mpg.de](mailto:Winkelmann@mpip-mainz.mpg.de)



“As we face distress we must not lose heart,  
stand fast and press on,  
triumph awaits.”  
*As I lay dying*



# Contents

<b>Zusammenfassung</b>	<b>vi</b>
<b>Abstract</b>	<b>vii</b>
<b>I. Introduction</b>	<b>1</b>
<b>II. Theory</b>	<b>5</b>
2.1. Point Groups & Crystal Classes . . . . .	6
2.2. Miller Indices . . . . .	10
2.3. Ferroics . . . . .	11
2.3.1. Symmetry Approach . . . . .	13
2.3.2. Thermodynamic Approach . . . . .	15
2.4. Perovskites . . . . .	19
2.4.1. MAPI . . . . .	19
2.5. Atomic Force Microscopy . . . . .	22
2.5.1. Working Principle . . . . .	22
2.5.2. Static & Dynamic Mode . . . . .	24
2.5.3. Piezoresponsive Force Microscopy . . . . .	27
2.5.4. Laser Doppler Vibrometer . . . . .	31
<b>III. Experiment &amp; Results</b>	<b>33</b>
3.1. Sample Preparation . . . . .	34
3.2. Temperature Calibration . . . . .	36
3.3. IDA Excitation . . . . .	38
3.4. Domain Characterization . . . . .	41
3.4.1. Vertical and Lateral Response . . . . .	41
3.4.2. Hysteresis Measurement . . . . .	43
3.4.3. Laser Doppler Vibrometer . . . . .	46
3.5. Domain Manipulation . . . . .	48
3.5.1. Mechanical Strain . . . . .	48
3.5.2. Slow vs. Rapid Cooling . . . . .	49
3.5.3. Electrical Switching . . . . .	51
<b>IV. Conclusion &amp; Outlook</b>	<b>55</b>
<b>A. Appendix</b>	<b>57</b>
<b>B. Bibliography</b>	<b>63</b>
<b>C. Acknowledgements</b>	<b>67</b>

# Zusammenfassung

Perowskite sind eine Materialklasse, die verschiedene interessante Eigenschaften aufweisen. Ein berühmtes von dieser Klasse abgeleitetes Beispiel ist Lanthan-Barium-Kupferoxid ( $\text{La}_{1,85}\text{Ba}_{0,15}\text{CuO}_4$ ) als Hochtemperatur-Supraleiter [MB87], oder Bariumtitanat ( $\text{BaTiO}_3$ ), was heute als Ferroelektrikum in Keramikkondensatoren verwendet wird.

Weiterhin gibt es auch photovoltaische Perowskite, die für die Herstellung von Solarzellen eingesetzt werden, insbesondere das in dieser Arbeit behandelte Methylammonium-Blei-Iodid ( $\text{MAPbI}_3$  oder MAPI). Perowskit-Solarzellen dieser Art können heute hohe Effizienzwerte von bis zu 25% [Nat19] erreichen, jedoch ist die genaue Ursache dafür noch nicht bekannt. Um diese herauszufinden macht es Sinn, die Nanostruktur der Perowskit-Schicht genauer zu untersuchen.

Eine Möglichkeit, diese Skalen sichtbar zu machen ist die sogenannte *Rasterkraftmikroskopie* (englisch: "Atomic force microscopy", AFM). Mit dieser Methode können kleinste Kornstrukturen im Perowskit sichtbar gemacht werden, aus denen die Schicht aufgebaut ist. Zusätzliche Modifikationen dieser Methode, wie beispielsweise die sogenannte *piezoresponsive Rasterkraftmikroskopie* (englisch: "Piezoresponsive force microscopy", PFM), ermöglichen es, weitere physikalische Oberflächeneigenschaften des Materials zu überprüfen. In diesem Fall wird gleichzeitig zur Topografiemessung ein lokales elektrisches Feld durch die Probe angelegt, wodurch elektro-mechanische Eigenschaften des untersuchten Materials sichtbar gemacht werden können.

Mit dieser Methode wurden in früheren Messungen charakteristische Strukturen sichtbar gemacht, die als *ferroelastische Zwillingsdomänen* identifiziert werden konnten [HBB<sup>+</sup>16]. Allerdings ist eine genauere Charakterisierung dieser Domänen noch nicht vollendet, ebensowenig der Zusammenhang zwischen ihnen und der hohen Effizienz der Solarzellen.

In dieser Arbeit wird die Natur der Zwillingsdomänen genauer erforscht. Hierzu werden externe Parameter wie Temperatur und mechanische Spannung gezielt verändert, um die Orientierung der Domänen zu manipulieren. Mit elektrischen Hysteresemessungen und lateral angelegten Feldern wird insbesondere die Frage behandelt, ob diese Domänen sogar ferroelektrischer Herkunft sind. Die hier durchgeführten Experimente sollen zu einem einheitlicheren Bild über die kristalline Struktur der Domänen und somit zu einem besseren Verständnis der Perowskit Solarzellen führen.

# Abstract

Perovskites are materials with different interesting properties. One famous example for the perovskite crystal structure is Lanthanum-Barium-copper oxide ( $\text{La}_{1,85}\text{Ba}_{0,15}\text{CuO}_4$ ), a high temperature supra conductor [MB87], or barium titanate ( $\text{BaTiO}_3$ ), used as ferroelectric in ceramic capacitors.

Furthermore, there are also photovoltaic perovskites for the fabrication of solar cells, especially methylammonium lead iodide ( $\text{MAPbI}_3$  or  $\text{MAPI}$ ), which is discussed in this thesis. Perovskite solar cells of this kind can reach efficiencies up to 25%, yet the specific cause for this performance is not known in detail. Therefore it makes sense, to have a closer look on the nanoscale of the perovskite layer.

One possibility to make these scales visible is the so called *atomic force microscopy* (AFM). With this method it is possible, to visualize the smallest grain structures in the material, from which the whole perovskite layer consists of. Furthermore, there are additional modifications of this method, e.g. the *piezoresponsive force microscopy* (PFM), which allow the investigation of further physical surface properties. In this case, an electric field is applied through the sample simultaneously to the topography measurement, in order to reveal the electro-mechanical response of the material.

In earlier measurements with this method, characteristic structures were made visible, which could be identified as *ferroelastic twin domains* [HBB<sup>+</sup>16]. A more precise characterization of these domains has not been completed yet, just as little as the relation between them and the high efficiency of the solar cells.

In this thesis the nature of the twin domains is explored more precisely. For this, external parameters as the temperature and mechanical strain are selectively changed, in order to manipulate the domain orientation. With electrical hysteresis measurements and laterally applied fields, the question if these domains are even ferroelectric, is embraced. The purpose of the performed experiments is to clarify, how the crystal structure of the domains looks like and thus to lead to a better understanding of perovskite solar cells.



# **I. Introduction**

One of the most important challenges in today's society is a sufficient energy supply for future generations. Presently, around 80% of the sources for our energy consumption are of fossil nature. These sources cause climate change, are finite and will be depleted one day [Int18]. In fact, the consumption peak will be already reached in the 2020's, so from there, the consumption compulsory decreases until the complete depletion [Ene18]. There is even a so called "Earth Overshoot Day", which symbolically indicates the day in the current year, when mankind consumes more resources, than our planet could restore in the same time. In the year 1990, this day was on December 7<sup>th</sup>, whereas in 2019 it was already on July 29<sup>th</sup>. With this background, it makes sense to turn towards renewable energy sources, such as wind and water, which are in principle infinitely available.

Among these inexhaustible sources is also the sun. From here, a radiation power of around  $18 \cdot 10^{16}$  W continuously reaches the earth. This is about 4 magnitudes more, than the worlds primary energy consumption [WW16], which means that there is theoretically more than enough energy to harvest.

One way to take advantage of the sun's energy is the use of solar cells, which convert the radiation into an electric voltage. State of the art research projects try to optimize the power conversion efficiency of these cells, extend their lifetime and make the manufacturing process less energy consuming.

A recent discovery for a different kind of solar cell are materials with a perovskite crystal structure. This arrangement of atoms is normally found in minerals, but when it is reproduced with the right elements, the resulting material can exhibit excellent photo responsive properties, like high charge-carrier diffusion lengths and low recombination rates, which is useful for the manufacturing of solar cells. In comparison to silicon cells, today's market leader, perovskite solar cells do not have to be built from high-purity monocrystals. This makes the fabrication process simpler and cheaper. Nevertheless, these cells are degrading relatively fast in ambient conditions, so that they are still subject of today's research.

In order to further optimize these devices, it is of great importance to understand as much of the material's nature as possible, e.g. charge transport mechanisms. Since these effects happen at the nanoscale, an appropriate observation method has to be chosen. The method, which is chosen in this thesis, is the atomic force microscopy (AFM), as well as a variation from it, the piezoresponsive force microscopy (PFM). With this method, a recent discovery of characteristic domain patterns in methylammonium lead iodide (MAPI) perovskites was made [HBB<sup>+</sup>16]. These domains appear in a periodic stripe pattern with an average width of around  $\sim 200$  nm. The alignment of the stripes within the solar cells can possibly have an influence on the charge transport, and thus on the efficiency of the whole cell. Therefore, it is reasonable to have a closer look on these patterns and get a better understanding on how to manipulate them.

There is a controversial debate in many groups, if these domains in MAPI are of a *ferroelectric* nature, additionally to it's already known *ferroelastic* behavior. This would imply, that besides from a different strain direction in adjoining domains, there would additionally be a differently oriented electrical polarization vector.



---

In this thesis, the ferroelastic twin domains of MAPI are measured with PFM and manipulated in different ways. Especially, the lateral switchability with an electric field is inspected, in order to critically examine the proposition of MAPI being ferroelectric.

**Chapter II** introduces the 32 point groups and crystal classes with the Hermann-Mauguin symbolism, as well as the meaning of Miller indices, in order to familiarize the reader with the notation used in the following sections. Subsequently the ferroic material class is presented, including two different theoretical approaches, which explain the appearance of domain states. The perovskite crystal structure is explained in more detail with the special case of MAPI, which is the main perovskite examined in this thesis. At the end of this chapter, the working principle of the main research methods, namely atomic force microscopy and piezoresponsive force microscopy, are explained.

**Chapter III** is the experimental part in this thesis. After shortly presenting the sample preparation procedure and preliminary calibration experiments, the domain pattern obtained with PFM is characterized. One experiment is the comparison between a lateral and a vertical excitation mode, which gives information about the crystal orientation within the domains. In order to check the ferroelectric character of the crystals, an electric hysteresis measurement is conducted. With a combination of the AFM setup and a Laser Doppler Vibrometer, the influence of disturbing cantilever dynamics on the PFM signal is inspected.

After the characterization follows a selective manipulation of the domains with several external quantities, such as mechanical strain and cooling rates. The final experiment is the in-plane switching of the domains with the application of a lateral electric field.

**Chapter IV** summarizes the gained knowledge and gives an outlook to possible experiments in the future.



## II. Theory

## 2.1 Point Groups & Crystal Classes

Point groups are a special type of group from the Euclidean geometry, which describe the symmetry of a finite object. Mathematically, this is described with the set of all possible symmetry operations, which map the object onto itself. These symmetry operations in the point groups always have at least one point, which is mapped onto itself. The possible operations are: *Identity mapping*, *point reflection* on a center of inversion, *mirroring* on a plane, *rotation* around a defined rotational axis as well as combinations of all of the above mentioned operations. When the consecutive execution of these operations is considered as an additive connection, a set of symmetry operations represents a *mathematical group*.

If one only considers three dimensional point groups, which are additionally consistent with an infinitely expanded lattice, one is left with 32 crystallographic point groups, also known as *crystal classes*. The more symmetry operations a point group has, the higher is the symmetry. The total number of symmetry operations defines the *order* of this point group. In the crystallographic field, mainly the *Hermann-Mauguin notation* is used to describe the point groups, where the symbols are defined as follows:

$p$	$p$ -fold rotation axis ( $p \in \mathbb{N}$ ): A rotation of $\frac{360^\circ}{p}$ around this axis leads to a symmetry equivalent object. Special cases are the identity with $p = 1$ , and $p = \infty$ , a rotation with an arbitrary small angle (e.g. the symmetry of a cone).
$\bar{p}$	$p$ -fold roto-inversion axis: A rotation of $\frac{360^\circ}{p}$ around this axis, with a subsequent point reflection ( $x' = -x$ , $y' = -y$ , $z' = -z$ ).
$m$	Mirror plane (e.g. for the $xy$ -plane: $x' = x$ , $y' = y$ , $z' = -z$ ).
$p/m$	$p$ -fold rotation axis with orthogonal mirror plane.

E.g. the  $2mm$  point group has a 2-fold rotation along the  $z$ -axis, with one mirror plane in the  $xz$ - and one in the  $yz$ - plane. Depending on the crystal class, the orientation of the symmetry axes and planes for the notation is set differently. Further details can be taken from the International tables for crystallography [HSA83].

In table 2.1 all crystal classes are shown with the corresponding symmetry group, figure 2.1 helps to visualize the symmetries. Additionally, the Schoenflies symbolism and the Laue group is given. Whereas the former one is mostly used for the description of molecule symmetries, the latter one is for the X-ray diffraction pattern classes. The last column breaks down to only 10 entries, since ordinary X-ray diffraction patterns are always centro-symmetric. Therefore, point groups with and without center of symmetry cannot be distinguished anymore.

The point group of a crystal is strongly connected to the macroscopic physical properties of the material. Examples for this phenomenon are optical transmission or mechanical strain. Generally, these properties are anisotropic, which means, that they depend on the direction of cause as well as on the direction of investigation. Therefore, these properties can be described with a physical tensor  $\sigma$ .

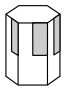
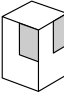
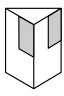
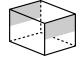
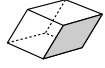
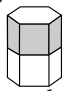
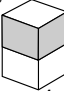
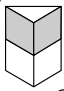
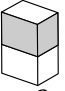
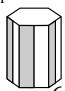
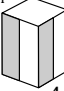
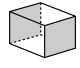
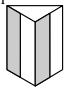
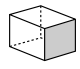
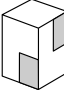
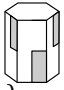
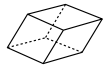
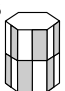
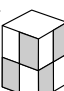
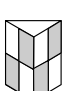
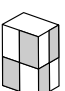
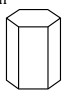
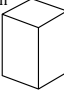
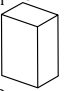
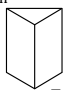
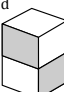
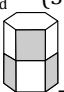
According to the so-called *Neumann's principle*, every symmetry operation of a material's point group must be a symmetry operation for  $\sigma$  as well. As a consequence, the independent components of  $\sigma$  can be reduced, and the principle axes are aligned with the crystal axes. This phenomenon also holds for the growth of the crystal. Therefore, the macroscopic shape of the material is already an indicator for the corresponding point group.

The other way around, one can predict possible physical properties with a known point group: E.g. if the point group has a center of inversion, a piezoelectric effect in this material is impossible. In this thesis, this is the case for the cubic phase of MAPI. When the point group changes because of a phase transition and loses this symmetry element, the piezoelectric effect can appear. This corresponds to the tetragonal phase of MAPI. For the following chapters, this is an important aspect, since the possibility of a piezoelectric effect is a requirement for *ferroelectricity*.

N°	Crystal Class	Schoenflies	Hermann-Mauguin	Laue Group
1	Triclinic	$C_1$	1	$\bar{1}$
2		$C_i$	$\bar{1}$	
3	Monoclinic	$C_2$	2	
4		$C_s$	$m$	
5		$C_{2h}$	$2/m$	
6	Orthorhombic	$D_2$	222	mmm
7		$C_{2v}$	2mm	
8		$D_{2h}$	mmm	
9	Tetragonal	$C_4$	4	$4/m$
10		$S_4$	$\bar{4}$	
11		$C_{4h}$	$4/m$	
12		$D_4$	422	
13		$C_{4v}$	$4mm$	
14		$D_{2d}$	$\bar{4}2m$	
15		$D_{4h}$	$4/mmm$	
16	Trigonal	$C_3$	3	$\bar{3}$
17		$C_{3i}$	$\bar{3}$	
18		$D_3$	32	
19		$C_{3v}$	$3m$	
20		$D_{3d}$	$\bar{3}m$	
21	Hexagonal	$C_6$	6	$6/m$
22		$C_{3h}$	$\bar{6}$	
23		$C_{6h}$	$6/m$	
24		$D_6$	622	
25		$C_{6v}$	$6mm$	
26		$D_{3h}$	$\bar{6}2m$	
27		$D_{6h}$	$6/mmm$	
28	Cubic	$T$	23	$m\bar{3}$
29		$T_h$	$m\bar{3}$	
30		$O$	432	
31		$T_d$	$\bar{4}3m$	
32		$O_h$	$m\bar{3}m$	

**Table 2.1.** The 32 point groups of the 7 crystal classes written in Schoenflies symbolism, Hermann-Mauguin notation and classified with the corresponding Laue group. The exact position of the symmetry axes in each class and further details can be taken from the International tables for crystallography [HSA83].

## 2.1. Point Groups & Crystal Classes

Schoenflies	Hexagonal	Tetragonal	Trigonal	Orthorhombic	Monoclinic	Triclinic	International
$C_n$	$C_6$  6	$C_4$  4	$C_3$  3		$C_2$  2	$C_1$  1	n
$C_{nv}$	$C_{6v}$  6mm	$C_{4v}$  4mm	$C_{3v}$  3m	$C_{2v}$  2mm			nmm (n even) nm (n odd)
$C_{nh}$	$C_{6h}$  6/m	$C_{4h}$  4/m			$C_{2h}$  2/m		n/m
	$C_{3h}$  $\bar{6}$				$C_{1h}$  $(\bar{2})$ m		$\bar{n}$
$S_n$		$S_4$  $\bar{4}$	$S_6$  $(C_{3i})$ $\bar{3}$			$S_2$  $(C_i)$ $\bar{1}$	
$D_n$	$D_6$  622	$D_4$  422	$D_3$  32 (V)	$D_2$  222			$n22$ (n even) $n2$ (n odd)
$D_{nh}$	$D_{6h}$  6/mmm	$D_{4h}$  4/mmm		$D_{2h}$ (mmm)  $(V_h)$ 2/mmm			$\frac{n}{m} \frac{2}{m} \frac{2}{m}$ (n/mmm)
	$D_{3h}$  $\bar{6}2m$						$\bar{n}2m$ (n even)
$D_{nd}$		$D_{2d}$  $(V_d)$ 42m	$D_{3d}$ ( $\bar{3}m$ )  $\bar{3} \frac{2}{m}$				$\bar{n} \frac{2}{m}$ (n odd)

**Figure 2.1.** Visualization of the 27 non-cubic crystallographic point groups [Kit05].

## 2.2 Miller Indices

Miller indices are an approach to uniquely describe crystal planes in a lattice. The notation was proposed in 1839 by William Hallows Miller [Mil39]. Next to describing possible crystal cleavages and twinning mechanisms, this notation is also used to represent lattice plane clusters in X-ray diffraction experiments. The construction of these indices is done as follows: At first, the plane has to be represented in the form

$$\vec{n} \cdot \vec{x} = 1 \quad , \quad \vec{n} = \begin{pmatrix} 1/s_1 \\ 1/s_2 \\ 1/s_3 \end{pmatrix} , \quad (2.1)$$

where  $\vec{n}$  is a normal vector, and  $s_i$  are the three axis interception points of the plane. Then,  $\vec{n}$  has to be multiplied with an integer  $j$  in such a way, that all components of  $\vec{n}$  become coprime integers:

$$\vec{n}_2 = \begin{pmatrix} j/s_1 \\ j/s_2 \\ j/s_3 \end{pmatrix} =: \begin{pmatrix} h \\ k \\ l \end{pmatrix} \quad (2.2)$$

The resulting components  $(hkl)$  are called *Miller Indices*. Negative numbers are indicated with a bar above the corresponding index. The most common planes are depicted in figure 2.2. For X-ray diffraction experiments, these indices are used for the reciprocal lattice vector  $\vec{G}_{hkl}$ :

$$\vec{G}_{hkl} = h\vec{g}_1 + k\vec{g}_2 + l\vec{g}_3 \quad (2.3)$$

With this representation and the so called *Laue-equations*, one can predict, under which conditions an X-ray is scattered on a selected crystal plane.

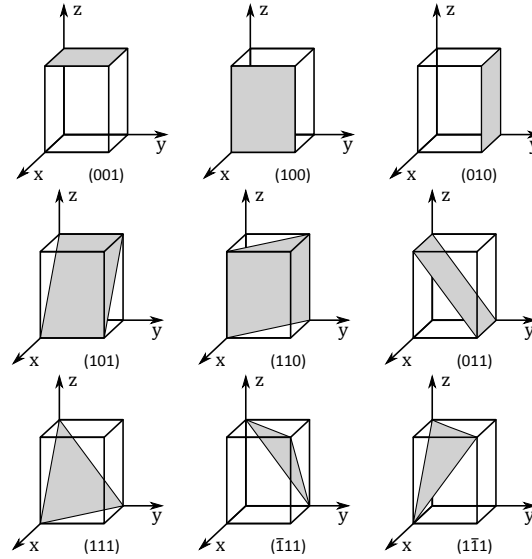


**Figure 2.2.** Visualization of the most common miller indices in an orthogonal rhombohedron. In crystallographic notation,  $x, y$  and  $z$  correspond to the  $a_1, a_2$  and  $c$  axis.



## 2.3 Ferroics

Ferroics are a class of materials, which show a spontaneous long range order, when going through a phase transition. The term was introduced by K  itsiro Aizu in 1970 [Aiz70], in order to universally describe the microscopic ordering behavior of *ferroelectric*, *-magnetic* and *-elastic* materials. In recent times, the *ferrotoroidic* class came up as well.

The term *ferro-* suggests, that the effect can be traced back to the presence of iron atoms [Bee14]. However, this is just a historical artifact, since researches began with the most prominent class, the *ferromagnetics*, where iron is a representative candidate. When the research expanded into the fields of electricity and elasticity, the term *ferro* was retained, in order to indicate a similar behavior as in magnetism.

A characteristic property of ferroic materials is the switchability of the long range order through an external force field, as well as the presence of a hysteresis curve. E.g. in a ferromagnetic material, the long range order is a collective alignment of magnetic moments, which can be switched with an external magnetic field. The microscopic properties from the other classes, the so called *primary ferroics*, can be taken from figure 2.3.

Type	Microsc. property	Force field	Schematic
Ferroelectric	El. dipole moment	E-field	
Ferromagnetic	Magnetic moment	B-field	
Ferrotoroidic	Magnetic vortex	Toroidal field	
Ferroelastic	Deformation	Stress	

**Figure 2.3.** Types of primary ferroics and their corresponding properties.

While the ferroelectric, -magnetic, and -toroidic deformations are defined by a vector, the ferroelastic strain is described by a symmetric second rank tensor [Sch08]. Besides these primary classes, there are also secondary and tertiary ferroics, which unite two or three different properties together.

As mentioned in the beginning, the ferroic ordering arises, when the material goes through a phase transition. In terms of symmetries, this means that the material is cooled from a higher symmetry crystal structure to one with lower symmetry. In this phase, a characteristic domain pattern appears, which can be observed with different physical measurement techniques.

## II. Theory

---

In the following sections, two different approaches are introduced, where the appearance of domain states is theoretically described. The first approach is based on the change of symmetry in the crystal's unit cell during the phase transition. The second one uses the Landau Theory, which minimizes the total energy of the system.

### 2.3.1 Symmetry Approach

For the symmetry approach, the phase with the higher symmetry is denoted as the “parent phase”  $G$ , and the lower symmetry phase as the “daughter phase”  $F$ . These letters stand as symbols for two out of the 32 point groups, which are presented in section 2.1. For  $F$  and  $G$  the group-subgroup relation holds:

$$F \subset G \quad (2.4)$$

In a ferroic phase transition, the parent phase unit cells get distorted in such a way, that the symmetry of  $G$  is lowered. Depending on the distortion, the transition can be classified as *distortive* or *reconstructive* [GM71]. In the latter case, the chemical bonds of the material are broken and reconstructed in a different way, so that only the chemical composition stays the same. In the former case, the crystal is systematically distorted, without disrupting any connections of the network. In the case of MAPI, the phase transition is distortive.

In Perovskite crystals, the asymmetry in the daughter phase can be caused by several changes. One of them is a shift of the central atom along the c-axis, which will be assumed in the following. When a spontaneous<sup>1</sup> polarization  $P_S$  is induced by this shifting, the associated phase transition is called *ferroelectric*. The symmetry loss from  $G$  to  $F$  is compensated by forming two or more equivalent configurations in the daughter phase. With the polarization, which can be described by a vector, e.g. in  $z$ -direction, one can now determine the number of possible configurations, which can appear in  $F$ . When the transition  $m\bar{3}m - 4mm$  is considered, one has to apply all the symmetry operations of the point group  $m\bar{3}m$  to the polarization vector. The operations, which are common with the  $4mm$  group, leave the vector  $P_S$  unchanged, whereas the uncommon operations transform it in different directions. In this case, there are five additional states, which differ in the orientation of  $P_S$ . This is schematically shown in figure 2.4. All the obtained states together are called the *ferroelectric domain states* of this certain species.

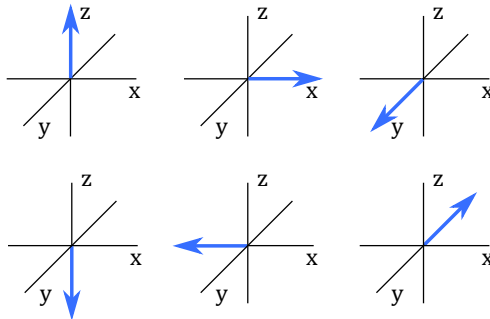


**Figure 2.4** Six possible directions for the spontaneous polarization  $P_S$  in the phase transition  $m\bar{3}m - 4mm$ .

<sup>1</sup>In this context, the term *spontaneous* implies a structural change without any external force fields.

## II. Theory

---

When the transformations can not be obtained as easily as in the example from above, there is a different way to determine the number of possible domain states  $q$ : When  $|A|$  is the order of the point group  $A$ , which counts all possible symmetry operations (including the identity),  $q$  can be calculated via

$$q = |G|/|F|. \quad (2.5)$$

In this example, one can verify that  $|G| = 48$  and  $|F| = 8$ , so  $q = 6$ .  $q$  is also known as the *index of  $F$  in  $G$*  [TCF10].

For simplification, the ferroelectric case with the polarization as a microscopic property has been discussed until now. Nevertheless, the idea behind it can be projected to any kind of ferroics as well, including ferroelastics. With the possible domain states in mind, it is obvious, that a suitable field vector (or stress tensor), can shift one state into another one, since it influences the energetically most favorable state of the domain orientation. This state shifting process is illustrated in figure 2.5. For the sake of clarity, a two dimensional phase transition with only two states is presented.

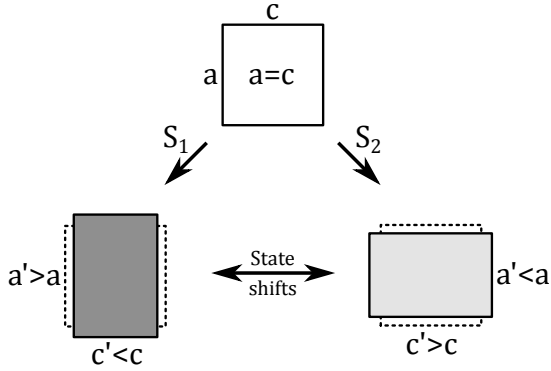


**Figure 2.5** State shifting process: In the 2D cubic to tetragonal phase transition, two states  $S_1$  and  $S_2$  can arise with the same probability. According to free energy considerations [Wad82], the transformation from one state to another can happen with a suitable external field.

### 2.3.2 Thermodynamic Approach

A different approach to describe the appearance of domains is the so called *Landau Theory*. It is the very first application of group theory in thermodynamics and is a description for physical phase transitions [Lan37]. The Landau Theory is a phenomenological approach, which does not give any predictions about microscopic causes, but is rather a consistent model for the macroscopic effects around the phase transition.

The concept behind it is a polynomial expansion of a thermodynamic potential  $\Phi$  as a function of a so called *order parameter*  $\eta$ . This parameter measures the degree of order in a system, when it goes through a phase transition. In more detail, it arises from a lowering of the symmetry from  $G$  to  $F$ , which is also known as *symmetry breaking*. In this situation, this one extra variables becomes necessary, to still be able to describe the state of the system. Consequently, it is defined in such a way, that  $\eta = 0$  in the  $G$ -phase, and  $\eta \neq 0$  in the  $F$ -phase. Depending on the order of phase transition, the value of  $\eta$  either changes continuously (2<sup>nd</sup> order) or discontinuously (1<sup>st</sup> order).

In the following, the case of a ferroelectric phase transition is considered with the polarization  $P_i$  as order parameter [TCF10]. For simplification, only one component of  $P_i$  is regarded, i.e.  $P_z$ .  $\Phi$  is the so called Gibbs energy, which is a function of polarization  $P_i$  and stress  $\sigma_{ij}$  as independent variables. It's differential is expressed as

$$d\Phi = E_i dP_i - \varepsilon_{ij} d\sigma_{ij}, \quad (2.6)$$

since a differential of a thermodynamic potential is, per definition, a function of the differential of it's independent variables. Here,  $E_i$  is the electric field and  $\varepsilon_{ij}$  is the strain tensor. From this expression, the following equations of state are derived:

$$\left( \frac{\partial \Phi}{\partial P_i} \right)_\sigma = E_i \quad , \quad \left( \frac{\partial \Phi}{\partial \sigma_{ij}} \right)_P = -\varepsilon_{ij}. \quad (2.7)$$

The general expansion of  $\Phi$  with respect to the order parameter  $P_z$  is

$$\Phi = \Phi_0 + \frac{1}{2}\alpha P_z^2 + \frac{1}{4}\beta P_z^4 + \frac{1}{6}\gamma P_z^6 + \dots, \quad (2.8)$$

whereas  $\Phi_0$  is the part of the equation, which is  $P_z$ -independent. In order to describe a phase transition of 2<sup>nd</sup> order, which applies to ferroics, the so called *Landau conditions* and the *Landau-Ginzburg criterion* have to be fulfilled. Therefore, the expansion only contains even powers of the order parameter. For a temperature driven transition, one sets

$$\alpha = \alpha_0(T - T_0), \quad \alpha > 0. \quad (2.9)$$

## II. Theory

---

For the description of a 2<sup>nd</sup> order phase transition, one sets  $\beta > 0$  and only considers the first two terms, so that the expression for the potential reads

$$\Phi = \Phi_0 + \frac{1}{2}\alpha P_z^2 + \frac{1}{4}\beta P_z^4. \quad (2.10)$$

With equation 2.7, this results in the equation of state for the order parameter:

$$E_z = \alpha P_z + \beta P_z^3 \quad (2.11)$$

For  $E_z \stackrel{!}{=} 0$ , the solutions for this equation describe the appearance of spontaneous polarization without any electric field:

$$P_z = \begin{cases} 0 & T > T_0 \\ \pm P_s := \pm(\alpha_0(T_0 - T)/\beta)^{1/2} & T < T_0 \end{cases} \quad (2.12)$$

One can see that for  $T > T_0$ , there is no spontaneous polarization, which means that the parent phase  $G$  is non-polar. For the regime  $T < T_0$ , the solution  $P_z = 0$  is unstable. Instead, the order parameter prefers to attain two values  $\pm P_s$ , corresponding to the two domain states, which appear in the daughter phase  $F$ . This temperature dependency for the thermodynamic potential is illustrated in figure 2.6. Both of the

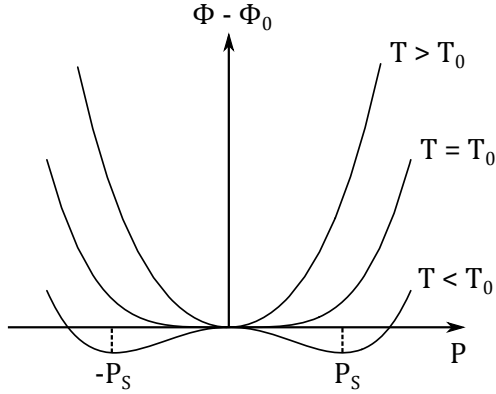


**Figure 2.6** Thermodynamic potential for a ferroelectric second order phase transition: At  $T < T_0$ , two degenerated energy minima appear at  $P = P_s$  and  $P = -P_s$ .

domain states have the same value for the Gibbs energy, namely

$$\Phi_F = \Phi_0 - \frac{\alpha_0^2}{4\beta}(T_0 - T)^2 \quad (2.13)$$

which means, that they are degenerate in energy. Consequently, the transition into either one of these states occurs with the same probability.

In this solution, the resulting polarization states are not coupled to an externally applied electrical field. If one wants to include this case as well, the thermodynamic potential has to be modified to  $\tilde{\Phi}$ . Care has to be taken, that  $\tilde{\Phi}$  leads to identical equations of state for the given variables. A suitable choice for  $\tilde{\Phi}$  is

$$\tilde{\Phi} = \Phi - P_i E_i \quad (2.14)$$

with it's differential

$$d\tilde{\Phi} = -P_i dE_i - \varepsilon_{ij} d\sigma_{ij}. \quad (2.15)$$

Following from this, the modified Gibbs energy including an electric field  $E_z$  is expressed as

$$\tilde{\Phi} = \Phi_0 + \frac{1}{2}\alpha P_z^2 + \frac{1}{4}\beta P_z^4 - P_z E_z. \quad (2.16)$$

The two stable solutions  $P_{\uparrow\uparrow}$  and  $P_{\uparrow\downarrow}$  correspond to the domain states with parallel and antiparallel orientation with respect to  $E_z$ . If the applied field is small enough so that

$$|P_{\uparrow\uparrow}| - P_s \ll P_s \quad (2.17)$$

$$P_s - |P_{\uparrow\downarrow}| \ll P_s, \quad (2.18)$$

is fulfilled, the energies of these states can be calculated as

$$\tilde{\Phi}_{\uparrow\uparrow} = \Phi_F - P_s E_z \quad \text{and} \quad \tilde{\Phi}_{\uparrow\downarrow} = \Phi_F + P_s E_z. \quad (2.19)$$

Now, the polarization with parallel orientation has a smaller energy and is therefore preferred. This also means, that domains in the a non-preferred state can in principle be switched into the preferred one, in the presence of an electric field. At a certain field strength, the so called *thermodynamic coercive field*  $E_{\text{crit}}$ , some states become instable and prefer to align with the electric field. This concept is sketched in figure 2.7, a so called *ferroelectric polarization-field hysteresis loop*. The interval between

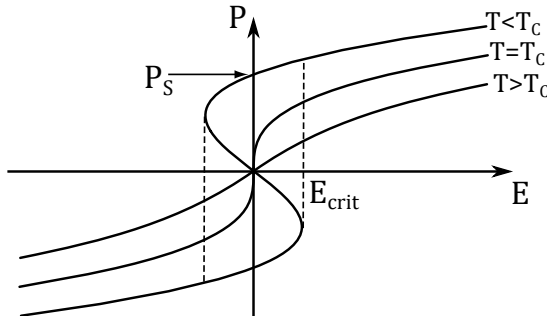


**Figure 2.7** Electric field dependency of the Polarization: At  $T < T_c$ , the stable part of the curve ( $\frac{\partial P}{\partial E} > 0$ ), together with the vertical dashed lines, represents a ferroelectric polarization-field hysteresis loop.

$-E_{\text{crit}}$  and  $+E_{\text{crit}}$  is instable and can switch to either the upper or the lower part of the  $P(E)$  curve, where  $\frac{\partial P}{\partial E} > 0$ , and the curve is stable. These parts together with the dashed lines make up the hysteresis loop.

## II. Theory

---

This derivation is a simplified model, which demonstratively explains the appearance of two one dimensional domain states in a ferroelectric material. In order to predict experimental observations in more detail, one can expand the calculations, e.g. by including all three dimensions and consider all components of the stress tensor as well, so that the ferroelastic part is also incorporated. However, since this would lead to too extensive calculations, this section remains with the most essential part, which is already covered.

One more aspect, which has to be considered, is the interface to the substrate, where the crystals are grown upon. Here, the misfits between substrate's surface and the crystals are another important factor: Because of this phenomenon, the system has to compensate the resulting strain and therefore creates ferroelastic domains [SP94]. Based on this concept, it is possible to calculate the minimal strain energy with several parameters, and see, which domain pattern is favorably built up. Depending on the transition type and different environmental parameters, often a pattern is preferred, which periodically changes between two opposingly polarized domains.



## 2.4 Perovskites

The perovskite crystal structure is one of the most common structures on planet earth, which was originally discovered in minerals. This material class makes up 93% of the lower mantle's mass and 38% of the total mass of the whole planet [SG17]. There are many different kind of perovskites, whereas every one shares the same crystal structure, shown in figure 2.8. The general chemical formula is denoted as  $ABX_3$ . In the cubic phase, the A-atoms are in the corners of the unit cell, the B-atom is at the body-centered position and the X-atoms are on the face centered positions. Even if

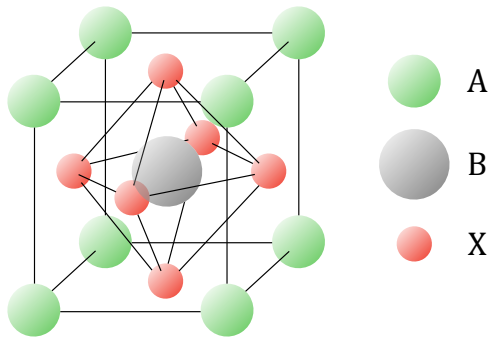


**Figure 2.8** The general atomic structure in perovskite crystals, here shown in the cubic phase.

this structure is so common, it can reveal interesting physical properties, when it is synthesized with the right atoms. E.g. metal halide perovskites can be used as solar cells due to their photosensitive nature [WHTC<sup>+</sup>18]. Some materials even reveal a ferroic behavior, such as barium titanate ( $BaTiO_3$ ), and thus are used as a ferroelectric in ceramic capacitors.

In the following, one special material composition is presented, which will be the main perovskite crystal in this thesis.

### 2.4.1 MAPI

Methylammonium lead iodide ( $MAPbI_3$ , or MAPI), is a chemical compound, which belongs to the organic-inorganic metal halide subclass, and is an example for photovoltaic perovskites. Here, the organic methylammonium cations ( $CH_3NH_3^+$ ) are at the A-positions, the metallic lead cation ( $Pb^{2+}$ ) is at the B-site and the halidic iodide anions ( $I^-$ ) stands for the X-atoms.

In total, MAPI can exist in three different phases, which are temperature dependent: The first one with the lowest symmetry ( $2mm$ ) has a orthorhombic structure. At 165 K ( $-108, 15^\circ C$ ), the atoms go through a first order phase transition into a tetragonal structure ( $4mm$ ), which is stable up to 327 K ( $53, 85^\circ C$ ). At this point there is a second order phase transition into the cubic structure, which has the highest symmetry ( $m\bar{3}m$ ).

## II. Theory

The relative ion sizes have to be matched very precisely, in order to keep the perovskite structure stable. Since the atoms in MAPbI<sub>3</sub> do not fulfill this criteria perfectly, the PbI<sub>6</sub> octahedra are slightly tilted and twisted, in order to stabilize the crystal structure. Hereby, no atomic bonds are broken apart. The crystal structure in the different phases can be taken from figure 2.9.

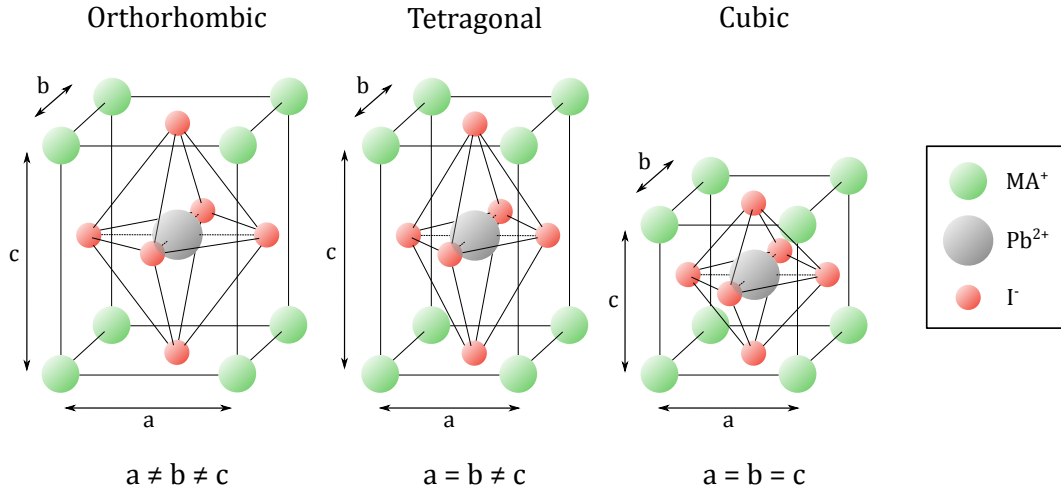


**Figure 2.9.** Crystal structures of MAPbI<sub>3</sub>: Orthorhombic ( $2mm$ ), tetragonal ( $4mm$ ) and cubic ( $m\bar{3}m$ ). Since  $a = b$  in the tetragonal structure, these lattice constants are also denoted as  $a_1$  and  $a_2$ .

In fact, the orthorhombic and the tetragonal phases have a higher point group symmetry than the ones mentioned above, namely  $2/mmm$  and  $4/mmm$  respectively. However, due to the shift and ordering of certain atoms in one preferred direction of the  $c$ -axis, the mirror plane perpendicular to this axis gets lost and the symmetry reduces from  $2/mmm$  to  $2mm$  and from  $4/mmm$  to  $4mm$ . This asymmetrically induced dipole is the cause for an electrical polarization in these phases. There are mainly three different possibilities, which could be the cause for this appearance: (1) an off-center shift of the Pb<sup>2+</sup> cations in the PbI<sub>6</sub> octahedral [FBW14], (2) a displacement of the MA<sup>+</sup> cations and (3) the orientation polarization of the MA<sup>+</sup> dipole [FXS<sup>+</sup>15].

Based on the theoretical concepts presented up to now and on previous experimental data, the patterns in figure 2.10 show some possible domain orientations for the  $m\bar{3}m - 4mm$  phase transition, where the arising polarization vector  $\vec{P}$  in the unit cells is assumed to point along the  $c$ -axis.

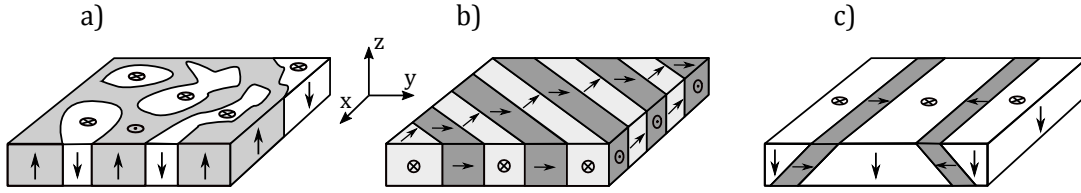


**Figure 2.10.** Selection of possible domain orientations in the  $m\bar{3}m - 4mm$  phase transition species. The arrows indicate the direction of spontaneous polarization  $\vec{P}$ . a) *c*-pattern, b)  $a_1/a_2$ -pattern, c) *a/c*-pattern.

In figure 2.10 a) the so called *c-pattern* is shown, where  $\vec{P}$  is periodically oriented parallel and anti-parallel to the substrate surface vector (here in  $z$ -direction). These domains have a bulky, non-geometric shape and have mostly been observed in samples, which are chemically etched [SMD93].

In contrast to that case, figure 2.10 b) and c) have also been observed in PFM measurements, which is the relevant method in this thesis. The pattern in b) is called  $a_1/a_2$ -pattern, because the vector  $\vec{a}_1 + \vec{a}_2$  is parallel to  $\vec{z}$ , while  $\vec{c}$  lies in the  $xy$ -plane. Expressed with Miller-Indices, the (110)-plane is parallel to the substrate surface. This pattern has equidistant domains, and furthermore, adjoining areas with different stripe orientations are connected in a  $90^\circ$  angle. The last picture in c) is a combination of *a*- and *c*-domains, therefore the *a/c-pattern*. KS Lee et al. observed the *a*-domains as lens-shaped, embedded in a larger *c*-domain [LCLB01].

In the latter two cases, the polarization vectors of neighboring domains are connected in a specific way: At the domain walls, the head of one vector always points at the tail of the other one. Consequently, this is called a *head-to-tail configuration*. This positioning of the unit cells ensures an electrical neutrality at the domain walls and is therefore energetically preferred. It has been observed on perovskite crystals with the same type of phase transition as well [Mer54][HM55].

Depending on the method of measurement, the flow of free charge carriers can be induced into the system. Therefore, the polarization configuration can also change to a head-to-head and a tail-to-tail one. The electrical neutrality is then only fulfilled on average over a larger area of domains. With this idea, it would be generally possible, that the domain pattern obtained by PFM arises only, when the polarization direction is induced by the measurement itself, and disappears again, when it is completed.

Furthermore it is predicted by A.K. Tangantsev et al., that global electrical switching of a large area is not possible, since this would drastically increase the elastic energy in the system. Nevertheless, a local switching of domains is possible, when the crystal grains have dimensions comparable to it's thicknesses [TCF10].

In order to investigate these domains on the nano scale, an appropriate method of measurement is necessary. In the following sections, the working principle of atomic force microscopy and further methods based on this technique are presented.

## 2.5 Atomic Force Microscopy

In today's research, the investigation of nanoscale phenomena is getting more and more important. Electronic devices like memory chips are designed in this scale in order to improve the computer performance. Generally speaking, the properties of macroscopic materials are determined by the structure in nano or even atomic scales. One device, which gives the opportunity to explore this world in the nanoscale is the so called *Atomic Force Microscope* (AFM). Even if it was already developed in 1985 [BQG86], it is still state of the art equipment for today's research. Besides just scanning the surface topography, the setup can be versatily modified in order to examine further material properties. One of these modifications, which will also be discussed in this section, is the application of an electric field between the microscope tip and the sample surface. This method is called *Piezoresponsive Force Microscopy* (PFM), which reveals electromechanical properties of the examined material. In the following section, the basic working principles of these two methods are explained, beginning with the original version of Atomic Force Microscopy.

### 2.5.1 Working Principle

The working principle of an AFM is illustrated in figure 2.12. The centerpiece, being the only direct connection between the microscope and the sample surface, is a sub-millimeter sized *cantilever* with a sharp tip at one end (tip radius  $\approx 25$  nm). By scanning this tip across the surface in a two dimensional square, the bending of the cantilever adapts to the changes in topography, due to the repulsive force of the surface. From the backside of the cantilever a laser is reflected onto a space resolved four quadrant photo diode. With this configuration, the cantilever movement is converted into a time dependent voltage. As opposed to Scanning Tunneling Microscopy (STM), the sample does not necessarily have to be conductive, since the scanning over the surface is purely mechanical and does not rely on any electric tunneling current, as used in STM.

For the scanning process, the laser deflection from the cantilever has to be set to a fixed value, the so called *set point*. This position, which also corresponds to a fixed tip-sample force, is the zero point for the feedback electronics. If the tip now moves over a topographical hump, the photo diode registers a change from this position and an error signal is transferred to the AFM controller. With this signal, the  $z$ -position of the piezo stage is adjusted and the cantilever is again on the original set point.

In order to chose this set point adequately, one has to consider different interaction forces between the tip and the surface, that can act on the cantilever. This is illustrated in figure 2.11:

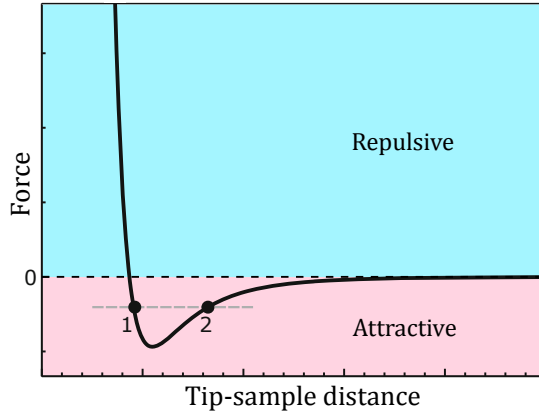


**Figure 2.11** Forces on the cantilever in dependence on the tip-sample distance: In the attractive regime (red) mainly electrostatic forces dominate. Very close to the surface, Pauli's Principle becomes relevant and the cantilever is repulsed (blue). At point 1 and 2, the same force magnitude acts on the cantilever [Voi15].

Coming from a large distance closer to the surface, the electrostatic force begins to attract the tip downwards. After overcoming a critical point, the force gradient changes the sign due to Pauli's principle, which postulates that two fermions can not exist at the same position. This leads to a repulsion of the cantilever. Because of this curve progression, the whole attractive regime is surjective. In this case it means, that there are always two tip positions, which lead to the same force value (except the cusp). Therefore one has to be careful to always measure on the same side of the slope, otherwise the signal gets unstable.

In order to get the amplitude values in nanometers instead of voltages from the photo diode, a resonance curve of the free oscillating cantilever is obtained. From here, the spring constant can be calculated, which is the necessary conversion factor.

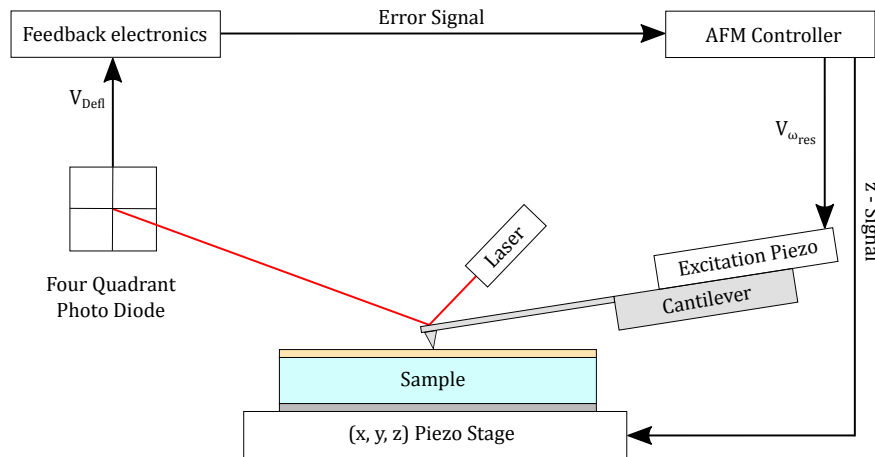


**Figure 2.12.** Working principle of an AFM: The four quadrant photo diode registers a deflection voltage ( $V_{Defl}$ ) and transfers it to the feedback electronics. From there, the corresponding error signal goes to the AFM controller, where the tip-sample distance is adjusted (z-Signal). Furthermore, the AFM controller sets the drive voltage for the excitation piezo, close to the cantilever's resonance frequency ( $V_{\omega_{res}}$ ).

### 2.5.2 Static & Dynamic Mode

The topography measurements with an Atomic Force Microscope mainly have two different scan modes: The first one is the so called *contact mode*. Here the set point is chosen in the repulsive regime, meaning that the tip actually touches the surface. The slight bending of the cantilever leads to a vertical deflection on the photo diode, which is then used as feedback signal.

However, if the set point is chosen too high and the same area is scanned many times, this method can possibly lose accuracy, because the tip starts scratching the sample surface. Furthermore, the tip can get blunt and collects pieces from the surface, so that the obtained images get distorted. For these reasons, there is a second and non destructive method, which is the *dynamic mode*. Here, the cantilever is constantly excited to a mechanical oscillation with a piezo element. For resonance enhancement, this excitation is chosen to be around the cantilever's resonance frequency. In this mode, the oscillation amplitude is used as feedback signal. Typically, the cantilever is now in the attractive regime around position 2 (see figure 2.11) and "taps" the surface at the lowest point. This is why this scan mode is also known as *tapping mode*. When the tip now approaches an obstacle, the force gradient changes the spring constant of the system. Furthermore, the damping coefficient increases, since tapping on a close obstacle damps the oscillation amplitude stronger. Both of these effects lead to a decreasing oscillation amplitude. This is registered by the AFM controller and consequently the height is adjusted.

In order to understand this response of the oscillation when approaching the surface, one has to model the cantilever movement mathematically with the equation of motion (EQM) of a driven harmonic oscillator. It is more convenient to start only with an excitation force  $F_{ext}(t)$  first, and later introduce the interaction between tip and sample. The classic EQM has the form

$$m\ddot{x} + d\dot{x} + kx = F_{ext}(t), \quad (2.20)$$

where  $m$  is the mass of the system,  $d$  is a constant in the friction term and  $k$  is the restoring force constant. On the other side of the equation,  $F_{ext}(t)$  is the external oscillating force, which has the form  $F_{ext}(t) = F_0 e^{i\omega t}$ . Introducing the resonance frequency  $\omega_0$  and a different friction constant  $\mu$  (for a more comfortable writing):

$$\omega_0 := \sqrt{\frac{k}{m}}, \quad \mu := \frac{d}{2m} \quad (2.21)$$

equation 2.20 transforms to

$$\ddot{x} + 2\mu\dot{x} + \omega_0^2 x = \frac{F_0}{m} e^{i\omega t}. \quad (2.22)$$

This EQM can be solved with the Ansatz  $x(t) = G \cdot e^{i\omega t}$  and leads to the condition

$$G = \frac{F_0/m}{\omega_0^2 - \omega^2 + 2i\omega\mu} \quad (2.23)$$

for the particular solution. Since the general solution is a damped oscillation and thus decays after a certain time, it is sufficient to only look at the obtained particular solution. With this expression, the frequency dependent amplitude  $A(\omega) = |G|$  and phase  $\Phi(\omega) = \arctan\left(\frac{\Im(G)}{\Re(G)}\right)$  of the system can be calculated:

$$A(\omega) = \frac{F_0/m}{\sqrt{(\omega_0^2 - \omega^2)^2 + (\omega\omega_0/Q)^2}} \quad (2.24)$$

$$\Phi(\omega) = \arctan\left(\frac{\omega\omega_0/Q}{\omega_0^2 - \omega^2}\right) \quad (2.25)$$

Here, the mechanical quality factor  $Q := \omega_0/2\mu$  is introduced, which is an indicator for the “sharpness and height” of the resonance. The results are a Lorentz function for the amplitude and an arc tangent function for the phase, which are also the two signals obtained by the AFM.

Now the distance dependent tip-sample interaction force  $F_{ts}(x)$  is added to the EQM:

$$m\ddot{x} + d\dot{x} + kx = F_{ext}(t) + F_{ts}(x) \quad (2.26)$$

Furthermore it is assumed, that this force varies only weakly in the scale of the oscillation amplitude. Therefore it can be written as a Taylor expansion around the equilibrium deflection point of the system:

$$F_{ts}(x) \approx F(x_0) + \left.\frac{\partial F}{\partial x}\right|_{x=x_0} \cdot (x - x_0) + \mathcal{O}(x^2) \quad (2.27)$$

The proportional term in  $x$  is interpreted as another spring constant

$$k' := \left.\frac{\partial F}{\partial x}\right|_{x=x_0}, \quad (2.28)$$

so that the modified equation 2.26 can be written as

$$m\ddot{x} + d\dot{x} + kx = F_{ext}(t) + F(x_0) + k'(x - x_0) \quad (2.29)$$

$$m\ddot{x} + d\dot{x} + (k - k')x = F_{ext}(t) + k\delta x - k'x_0 \quad (2.30)$$

whereas  $k\delta x$  and  $k'x_0$  are constant offsets and thus can be neglected. With the definition of a new effective spring constant  $k_{eff} := k - k'$ , the equation transforms to

$$m\ddot{x} + d\dot{x} + k_{eff}x = F_{ext}(t) \quad (2.31)$$

so it has the same shape as equation 2.20 in the beginning and therefore the same solutions, only with a shifted resonance frequency:

$$\omega_{eff} := \sqrt{\frac{k_{eff}}{m}} = \sqrt{\left(k - \frac{\partial F}{\partial x}\right)/m} \quad (2.32)$$

Depending on the sign of the force gradient, the frequency shift can be either positive or negative. For attractive potentials with  $\frac{\partial F}{\partial x} > 0$  follows  $\omega_{eff} < \omega_0$  and for repulsive potentials with  $\frac{\partial F}{\partial x} < 0$  follows  $\omega_{eff} > \omega_0$ .

## II. Theory

Since the resonance frequency is also related to the quality factor  $Q$ , a change of  $\omega_0$  results in a different height of the amplitude curve.

As it can be seen from the expression for  $\omega_{eff}$ , the resonance frequency shift is only dependent on the sample-distance force *gradient*. A spatially invariant force would only lead to an offset in the deflection of the cantilever, but leave  $\omega_0$  unchanged. The amplitude and phase resonance curves with different frequency shifts are represented in figure 2.13.

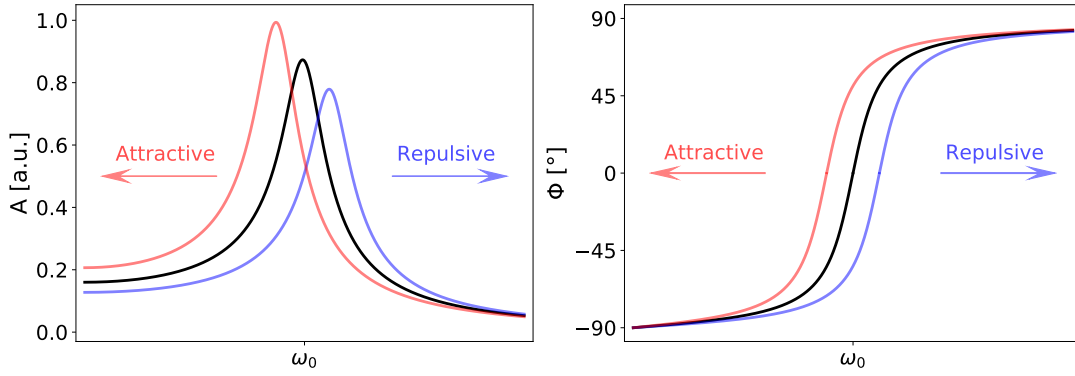


**Figure 2.13.** Amplitude and phase signal, according to equation 2.24 and 2.25. The red graphs represent an attractive potential, the blue ones are in the presence of a repulsive potential.

This derivation shows, that the resonance frequency of the cantilever can shift due to the presence of tip-sample interaction forces  $F_{ts}(x)$ . This effect is later referred to as “cantilever dynamics” and can also happen in contact mode. It is the chosen method for the experimental part, because it is necessary for piezoresponsive force microscopy. Therefore one has to keep in mind, that the actual electromechanical response from the surface can be superimposed by this resonance shift effect and cause an additional amplitude contrast.

In the following section, the working principle of piezoresponsive force microscopy is explained in more detail.



### 2.5.3 Piezoresponsive Force Microscopy

The working principle of Piezoresponsive Force Microscopy (PFM) is based in the inverse piezoelectric effect. Materials which have piezoelectric properties, deform mechanically when an electric voltage is applied. Therefore, the measurement requires a material with a non-centrosymmetric point group, so that this effect is possible. This requirement is fulfilled for the tetragonal phase of MAPI.

In order to use this effect in an atomic force microscope, an AC voltage is applied between the conducting cantilever and the grounded sample back electrode, in order to excite mechanical deformations in the material below the tip. For high electric fields, it is necessary to bring the tip as close to the surface as possible. Therefore, the measurement is operated in contact mode. Since the tip touches the surface in this confinement, the signal enhancement at the free resonance frequency  $\omega_{free}$  of the cantilever does not work anymore. Instead, the sample surface and the cantilever build a connected system with a different resonance frequency, which is called the *contact resonance frequency* ( $\omega_{cont}$ ). This is the chosen frequency, where the PFM signal is enhanced. According to [RJA96][YN98][KRP<sup>+</sup>00],  $\omega_{cont}$  is around 3 to 5 times larger than  $\omega_{free}$ , depending on the sample stiffness and several other parameters.

Generally, the piezoelectric effect is a anisotropic quantity, and can therefore be described with a second rank tensor:

$$d_{ij} := \begin{pmatrix} d_{11} & d_{12} & d_{13} \\ d_{21} & d_{22} & d_{23} \\ d_{31} & d_{32} & d_{33} \end{pmatrix} \quad (2.33)$$

The three diagonal entries  $d_{ii}$  are the magnitude of expansion in the  $x$ -,  $y$ - and  $z$ -direction. The off-diagonal components describe a shearing of a plane in a particular direction. The first index of these entries indicates the direction of the plane's normal vector, the second one is the direction of shearing. E.g.  $d_{31}$  is the shearing of the  $xy$ -plane in  $x$ -direction.

With PFM, the diagonal entries are detected in the vertical detection mode, the off-diagonal ones in the lateral mode. These two operations are illustrated in figures 2.14 and 2.15.

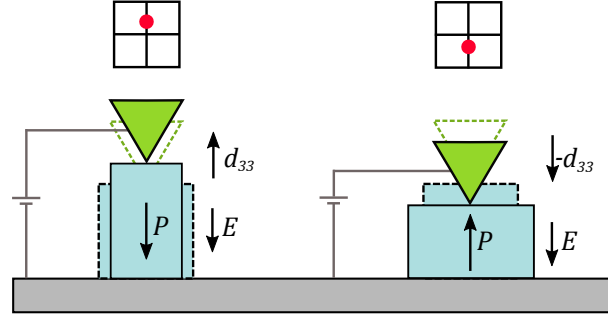


**Figure 2.14.** Vertical PFM: Depending on the orientation of the polarization  $\vec{P}$  with respect to the applied electric field  $\vec{E}$ , the material either expands or contracts. This can be described with the longitudinal piezoelectric coefficient  $d_{33}$ .

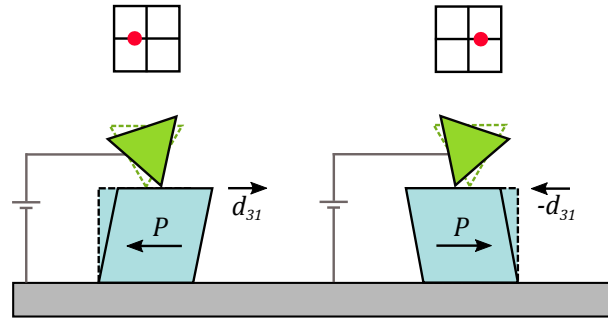


**Figure 2.15.** Lateral PFM: In this mode, the lateral piezoelectric response ( $d_{31}$  and  $-d_{31}$ ) is detected on the photo diode. Depending on the in-place polarization orientation, the system shears to the left or to the right.

For the vertical PFM, a non-zero out of plane polarization component has to be present in the examined material. If this polarization vector  $\vec{P}$  is parallel to the electric field vector  $\vec{E}$ , the effective piezoelectric response of the surface in z-direction  $d_{33}$  is positive and the domain expands. When  $\vec{P}$  and  $\vec{E}$  are anti-parallel,  $d_{33}$  is negative and the domain contracts. These two responses can be distinguished with the vertical deflection of the four quadrant photo diode.

In the lateral PFM mode, there has to be a non-zero in plane polarization component. Depending on the orientation, the material either shears to the left or to the right. This can be recognized by the lateral deflection signal of the photo diode, since the cantilever tip is dragged along with this movement. At the boundaries of two differently polarized domains, the piezoresponse cancels out and results in no signal on the photo diode.

The lateral contact resonance is even higher than the vertical one, namely around 12 times  $\omega_{free}$ . Since both of the contact resonances have a relatively small signal to noise ratio, it is necessary to enhance them with a lock-in amplifier (LIA). The modified setup with the AC voltage source and the LIA is represented in figure 2.16. As in the ordinary AFM setup from figure 2.12, an amplitude and phase signal can be extracted from the measurement. This time, the amplitude represents the movement of the cantilever due to the material excitation. In this setup, the root mean square value of the alternating deflection voltage is calculated ( $V_{rms}$ ). The phase value, calculated in angular degrees, is the shift between the excitation signal and the obtained cantilever movement. In order to distinguish these signals from the tapping mode  $A$  and  $\Phi$ , they are labeled here as  $R$  and  $\Theta$ .

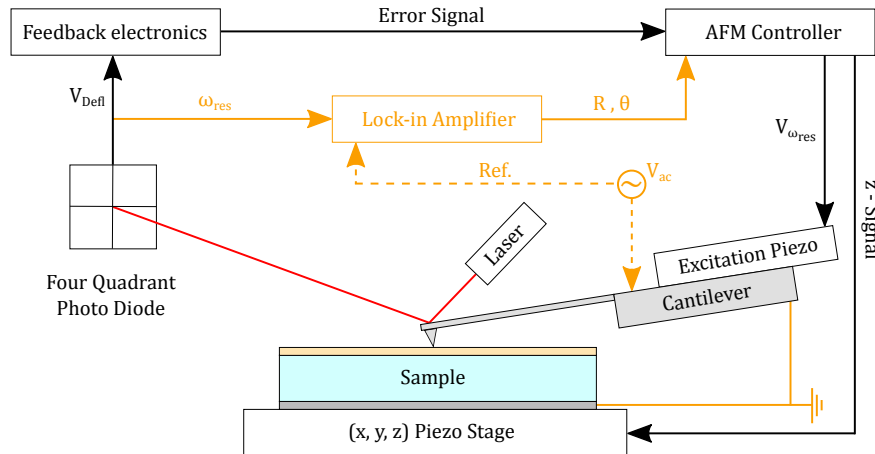


**Figure 2.16.** PFM setup: The sample surface is electrically excited with an AC voltage between the cantilever and the grounded back electrode. The contact resonance frequency  $\omega_{res}$  is enhanced with the lock-in amplifier and transfers the amplitude and phase signal ( $R$ ,  $\Theta$ ) to the AFM controller. The circuit diagram is shown in figure A.1.

## II. Theory

---

One further parameter which can be varied in the measurements is the cantilever scan direction. The default value is  $0^\circ$ , which means that the scan goes along the axis of the cantilever. It is also possible to set this value to  $90^\circ$ , so a scan direction perpendicular to the cantilever axis (and any other angle between  $0^\circ$  and  $360^\circ$ ). In some cases, this leads to a better image contrast within one scan line. Presumably, this has to do with the anisotropic cantilever stiffness as well as how the sample is oriented under the tip, with respect to the scan direction.

Besides this phenomenon, there are some other effects, which can influence the PFM signal and thus distort the correct interpretation of the obtained signal. In the following, the two most relevant effects are shortly mentioned [SKK17]:

One of them is the *electrostatic effect*, which appears between the cantilever and the sample surface. It is a Coulombic force, which can be described with

$$F_E(x) = \frac{1}{2} \frac{dC}{dx} V^2, \quad (2.34)$$

where  $C$  is the capacitance of the cantilever and  $V$  the total voltage between the latter and the surface. This is one example for a distant dependent external force  $F_{ts}(x)$ , which was added to EQM 2.26 and lead to a amplitude and frequency shift (see section 2.5.2). Even in contact mode, when the tip is already touching the surface, this effect influences the PFM signal, because the conducting cantilever is only a few micrometers distant from the surface.

The second effect is *electromechanical strain*. In ionically active materials, the application of an electric field can redistribute the ions locally underneath the cantilever tip. This motion precedes volume changes, which then move the laser deflection on the photo diode. The electromechanical strain depends on the magnitude  $V$  and frequency  $\omega$  of the applied AC voltage, as well as on the temperature  $T$ . In some materials it is possible, that these local ion redistributions can also be the origin of electrical hysteresis loops, even if there is no ferroelectricity present whatsoever.

Another variant, which can be applied to the PFM setup, is a combination with a so called *Laser Doppler Vibrometer* (LDV), which will be explained in the next section. With this device, it is possible to exclude the cantilever dynamics, which were explained in section 2.5.2, from the real piezoresponse.

### 2.5.4 Laser Doppler Vibrometer

A Laser Doppler Vibrometer (LDV) is a device, to determine the velocity in vibrating objects. The working principle is shown in figure 2.17. A laser beam is split into two parts: The first one goes directly onto a detector, while the second part is guided to the surface of the vibrating object. Afterwards, the reflected beam goes to the same detector, where the overlay of the two signals is analyzed.

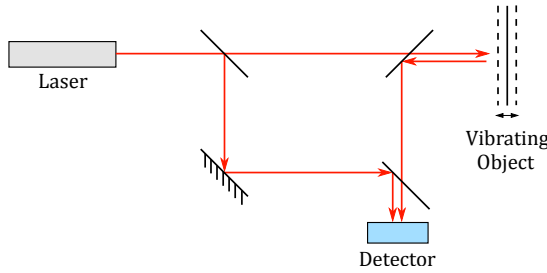


**Figure 2.17** Laser Doppler Vibrometer: A laser beam is split into two parts: The first one goes as reference signal onto a detector, the second one registers the vibration of an object and then goes to the same detector.

The main phenomenon in this device is the *Relativistic Doppler Effect*. Due to the movement of the vibrating object with velocity  $v$ , the laser frequency  $f$  is changed according to

$$f' = f \sqrt{\frac{c \pm v}{c \mp v}}, \quad (2.35)$$

whereas  $c$  is the speed of light. The top sign in this formula represents an approach of the object towards the observer, the bottom sign is for a receding object. In this case, the object moves alternately towards and away from the detector, so the modified frequency  $f'$  varies with time. When this slightly changed frequency signal is added to the unchanged one directly from the laser source, one gets a periodically in- and decreasing amplitude, also known as *beat signal*. From here, the velocity of the vibrating object can be extracted.

This method can be applied to the vibrational movement of a cantilever in contact mode: Instead of a conventional optical beam deflection laser (OBD), the LDV laser is applied and focused on the back of the cantilever. Then, the laser position is varied in such a way, that the signal from the cantilever vibration is minimized. This means, that the spot is now just above the cantilever tip, where the excitation vibrations vanish almost completely. In this configuration, the measurement is independent of the contact resonance. Therefore, all cantilever dynamics are excluded from the laser deflection and only real piezoresponsive movements of the sample surface contribute to the signal. This concept is illustrated in figure 2.18.

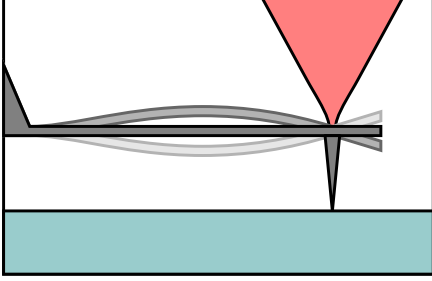


**Figure 2.18** LDV setup: The LDV laser is positioned just above the cantilever tip. This way, possible cantilever dynamics are excluded (Taken from [LP15]).

Earlier experiments by A. Labuda et al. [LP15] compared the OBD and the LDV method to one another. Therefore the measurements were applied to one reference sample, which was periodically poled lithium niobate (PPLN). This is a well known ferroelectric material, where neighboring out of plane polarizations are shifted by  $180^\circ$ . Furthermore the amplitude signal does not dependent on the polarization orientation of the domains. The comparison of the two methods on this sample is shown in figure 2.19.

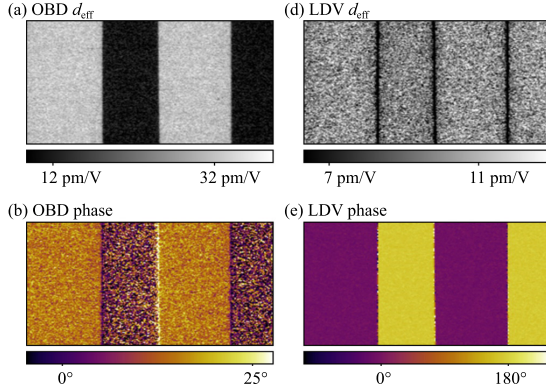


**Figure 2.19** Comparison of an OBD with a LDV measurement: The amplitude signals a) and d) are recalculated to the effective piezoelectric sensitivity  $d_{eff}$  of the surface.

The OBD amplitude signal in figure 2.19 a) shows a strong contrast of around 20 pm/V between the domains. The amplitude value is here recalculated in the piezoelectric sensitivity  $d_{eff}$  of the surface, which expresses how much the surface moves per applied voltage. At the same time, there is a weak phase contrast of around  $25^\circ$ . As a result, the OBD measurement is clearly not consistent with the previously known properties of the PPLN surface.

On the other hand, the LDV measurement reveals exactly the expected behavior of the domains: Almost no amplitude contrast between the domains (only around 4 pm/V) and a perfect phase contrast of  $180^\circ$ . The amplitude images shows very well, that the signal cancels out at the domain boundaries.

Consequently, the LDV measurement is a reliable method to detect real ferroelectric properties with an out of plane orientation, excluding all possible cantilever dynamics which could possibly superimpose the PFM measurement.

### III. Experiment & Results

In this chapter, several experiments are conducted in order to find out, if the ferroelastic twin domains in MAPI are also ferroelectric. Furthermore, the polarization orientation inside the domains is concluded from the obtained experimental results. The main experiment is an in plane switching of the domain orientation with a lateral electric field. When the domains change their orientation, the switching can be assigned to the presence of an electric polarization vector in the domains. From here it follows, that MAPI is ferroelectric.

For this purpose, the samples have to be prepared with a lateral electrode structure. At the beginning of this chapter, two variants with different switching electrodes are presented: The first one has an evaporated gold layer, whereas the second one has an interdigitated array of electrodes (IDA).

Before the investigation of the domains, two preliminary experiments were necessary: The first one is a series of PFM measurements on the same MAPI grain at different temperatures. Due to thermal motion, a higher temperature close to the phase transition temperature  $T_C$  promotes electrical switching. With the calibration process in this experiment, the temperature for the switching experiment can be set to  $T \lesssim T_C$ .

The second preliminary experiment is a series of different excitations on the IDA electrodes. This measurement makes sure, that the applied electric field actually affects the MAPI grains on top of it, even if they are insulated from the electrode structure.

After the preliminary experiments, the lateral and vertical PFM measurements on one grain are compared to one another. This measurement gives information about possible domain patterns. Then, an electrical hysteresis measurement is conducted, which is also a hint on ferroelectricity. A combined AFM and Laser Doppler Vibrometer setup excludes the effects of cantilever dynamics.

In the last section, several manipulation methods on the domains are conducted, including the electrical switching experiment.

### 3.1 Sample Preparation

In this section, the sample preparation of two different layering architectures for the electrical switching experiment is explained. The main feature for both variants is the presence of lateral electrodes, where the switching voltage can be applied.

The first variant is a glass substrate with a conducting Fluorine doped Tin Oxide (FTO) layer on top. This layer acts as the back electrode for the PFM measurements. This basic substrate is chosen, since it brings the back electrode as close as possible to the MAPI crystals. On top of the FTO is an insulating SiO<sub>2</sub> layer, followed by a gold film. The gold film is split by a 25 µm thick gap, so that the switching voltage can be applied between these two parts. The SiO<sub>2</sub> prevents the FTO from being short circuited with the gold electrodes. Finally, the MAPI crystals grow on top of this configuration. The sample and the corresponding layer thicknesses are illustrated in figure 3.1. Due to a better clarity, the layer thicknesses are not exactly true to scale.

The second variant is an Interdigitated Array (IDA) with platinum electrodes and an aluminum layer underneath as back electrode. Since the MAPI crystals only crystallized on top of the electrodes and not inside the gap, an additional SiO<sub>2</sub> layer is included. Additionally, this layer also acts as insulation between the electrodes and the crystals. On top of it, the MAPI layer is distributed homogeneously over the whole area. This sample and its layer thicknesses are shown in figure 3.2.

In the following, the fabrication process of these two samples is described in more detail:

For the synthesis of MAPI (MAPbI<sub>3</sub>), the precursor materials methylammonium iodide (CH<sub>3</sub>NH<sub>3</sub>I) and lead chloride (PbCl<sub>2</sub>, Sigma-Aldrich, 99.999%) were prepared as described in [HBB<sup>+</sup>16]. According to the reaction equation



the mass ratio of MAI to PbCl<sub>2</sub> was chosen to be 400 mg : 233 mg. This mixture was then diluted in 1 ml anhydrous dimethylformamide (DMF, Sigma) at 50 °C.

The FTO ( $R_s \sim 7 \Omega/\text{sq}$ ) as well as the IDA substrates were cleaned sequentially with 2% Hellmanex II, deionized water, acetone, and isopropanol in an ultrasonic tank. For the latter substrate, a platinum array was chosen, since it gives a cleaner PFM signal than the one with a gold array. Before sputtering the electrically insulating SiO<sub>2</sub> layer on top, both of the substrates were treated with O<sub>2</sub> plasma for 30 min, in order to make the surface more receptive.



For the FTO sample, a gold layer of 50 nm thickness was evaporated on top of the  $\text{SiO}_2$  layer with a deposition rate of  $1,2 \text{ \AA/s}$ . For the lateral switching experiment, the gold was separated into two parts by a  $25 \mu\text{m}$  thick gap. This gap was generated by a tungsten wire of the same thickness, which was fixed onto the desired position before mounting the sample in the gold evaporator. After that,  $150 \mu\text{l}$  of the MAPI solution were spincoated onto the substrate with 1750 rpm for 1 min. Then the sample was left to dry for 30 min in nitrogen atmosphere. For the single crystal fabrication, the sample was undergoing a solvent annealing process: Therefore it was placed on a  $100^\circ\text{C}$  hot plate together with two droplets of DMF close by. On top of that, a watch glass was placed close to the hotplate edge in a way, that the DMF could dissipate during the solvent annealing process. In this configuration, the substrates were left for 60 min.

For the IDA sample, the MAPI layering process was the same, except for the volume of the MAPI solution, which was only  $30 \mu\text{l}$ . Since only the small IDA area needed to be covered, there was much less solution needed for the spincoating process.

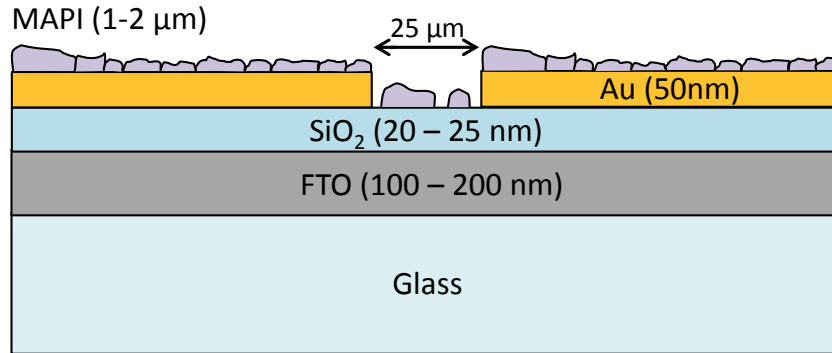


**Figure 3.1.** FTO sample

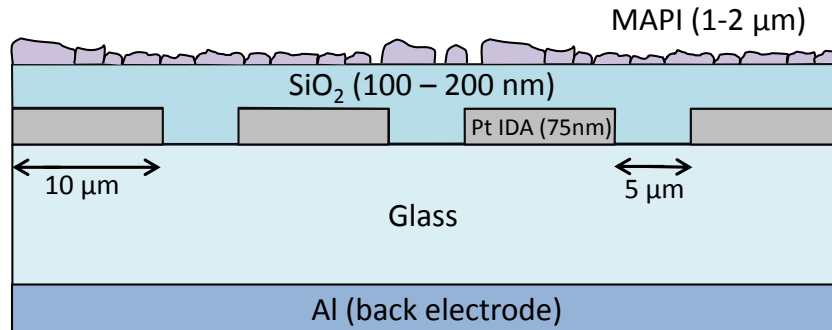


**Figure 3.2.** IDA sample

## 3.2 Temperature Calibration

Temperature has a significant role in the switching experiment. When approaching the phase transition temperature  $T_C$  from the tetragonal to the cubic phase, the thermal motion energetically promotes a possible switching event. Therefore, the temperature  $T$  in the switching experiment will be increased until  $T \lesssim T_C$ . The series of measurements in this section was taken, in order to find the approximate phase transition temperature  $T_C$  in the actual setup for the electrical switching experiment. This setup includes the Asylum Research heating stage, several heat conduction elements and the actual sample with a thermometer. The heat loss from the heating stage to the sample makes such a calibration process necessary. It guarantees, that  $T$  stays below  $T_C$ , otherwise it would erase the domain structure from the tetragonal phase and a random reorientation can take its place.

The PFM measurements in this and the following sections are executed with the MFP-3D Atomic Force Microscope (Asylum Research, England), set up in a nitrogen glovebox and combined with the HF2LI Lock-in Amplifier (Zurich Instruments, Switzerland). The detailed circuit diagram can be taken from A.1. As a cantilever, the SCM-PIT-V2 Platinum-Iridium coated model (Bruker, USA) is chosen. The spring constant is  $k = 3 \text{ N/m}$ , the free resonance frequency is  $f_0 = 75 \text{ kHz}$ .

Figures 3.3 to 3.6 show PFM phase images of *ferroelastic twin domains* on the same MAPI grain, when going beyond the phase transition temperature  $T_C = 53, 85^\circ\text{C}$ . The domains were fading, the more the temperature was increased. It is remarkable, that there is no abrupt disappearance right at  $T_C$ , but a rather continuous evanescence. The reason for this is that the heat of the hotplate is not distributed homogeneously in the whole crystal. A demonstrative example is, that the top of the crystal is further away from the heating source and thus is colder than the bottom. Therefore there are some regions, where the domains disappear more quickly than in other ones.

The disappearance of the domains in general is explained with the higher symmetry in the cubic phase. In this phase, the lattice constant  $c$  shrinks to the same magnitude as  $a$ . Therefore the polarization of the unit cell vanishes and the domains become indistinguishable.

In the calibration measurement, the domains are still visible at  $T = 50^\circ\text{C}$  and almost vanished at  $T = 55^\circ\text{C}$ . This observation is consistent with the known value of the phase transition temperature. For the switching experiment, the temperature will therefore be set to  $T = 50^\circ\text{C}$ .

### 3.2. Temperature Calibration

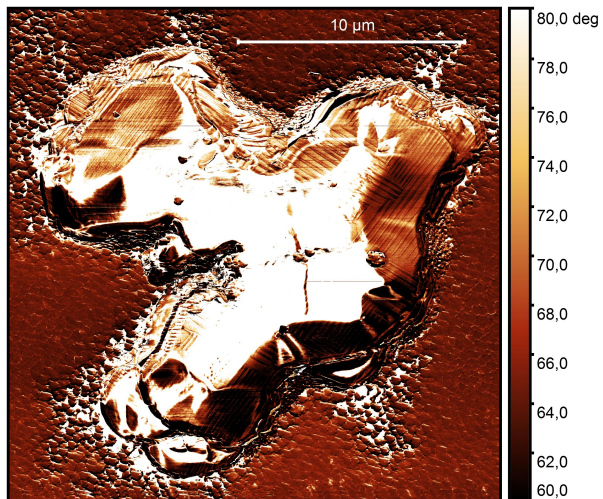


Figure 3.3.  $T = 27^\circ\text{C}$

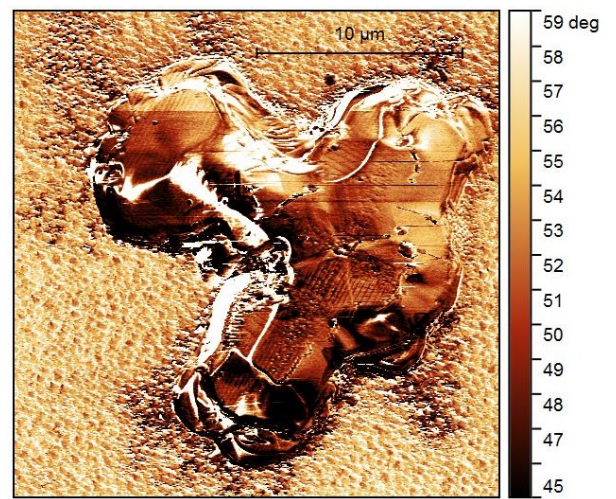


Figure 3.4.  $T = 40^\circ\text{C}$

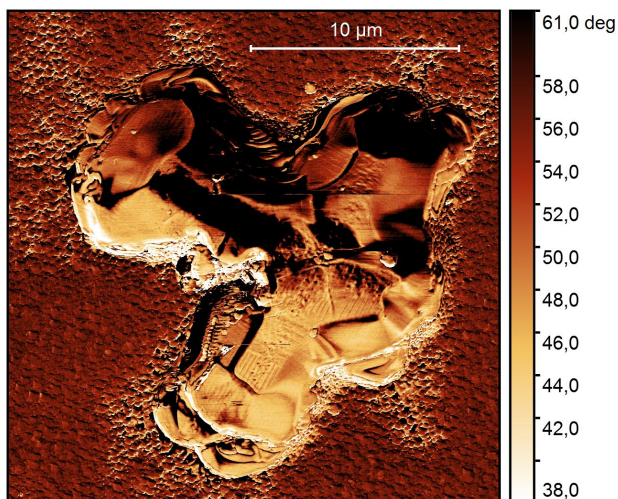


Figure 3.5.  $T = 50^\circ\text{C}$

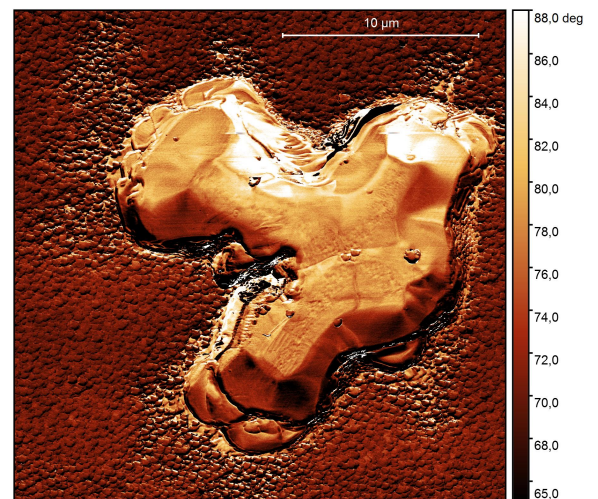


Figure 3.6.  $T = 55^\circ\text{C}$

## 3.3 IDA Excitation

This preliminary experiment tests, if the application of an electric field on the IDA electrode structure has a visible effect on the MAPI crystals above them. This is a requirement for the electrical switching experiment.

Normally, the AC-excitation voltage for PFM measurements is applied between the cantilever and the back electrode of the sample. In this experiment, the case is different: In order to distinguish between the two electrodes, the AC-voltage is applied to one of the electrode arrays, while the other one and the cantilever are grounded to the same potential. For the inverted polarization, the excitation is applied to the opposite electrode array. This concept is illustrated in figure 3.7.

For this experiment, a MAPI grain between two electrodes is needed, so that one can see, how the measurement is affected, when the electrode array with the excitation voltage is switched. As a result, the variation of the electrode polarization is well visible, as seen in figure 3.8. Even if there is an insulating  $\text{SiO}_2$  layer between the crystal and the electrode array, the applied field mainly changes the PFM signal on the crystal. Furthermore the color brightness on the crystal continuously decreases from one electrode to the other, which indicates the direction of the electric field.

This qualitative experiment confirms the suitability of the IDA sample for the electrical switching experiment.

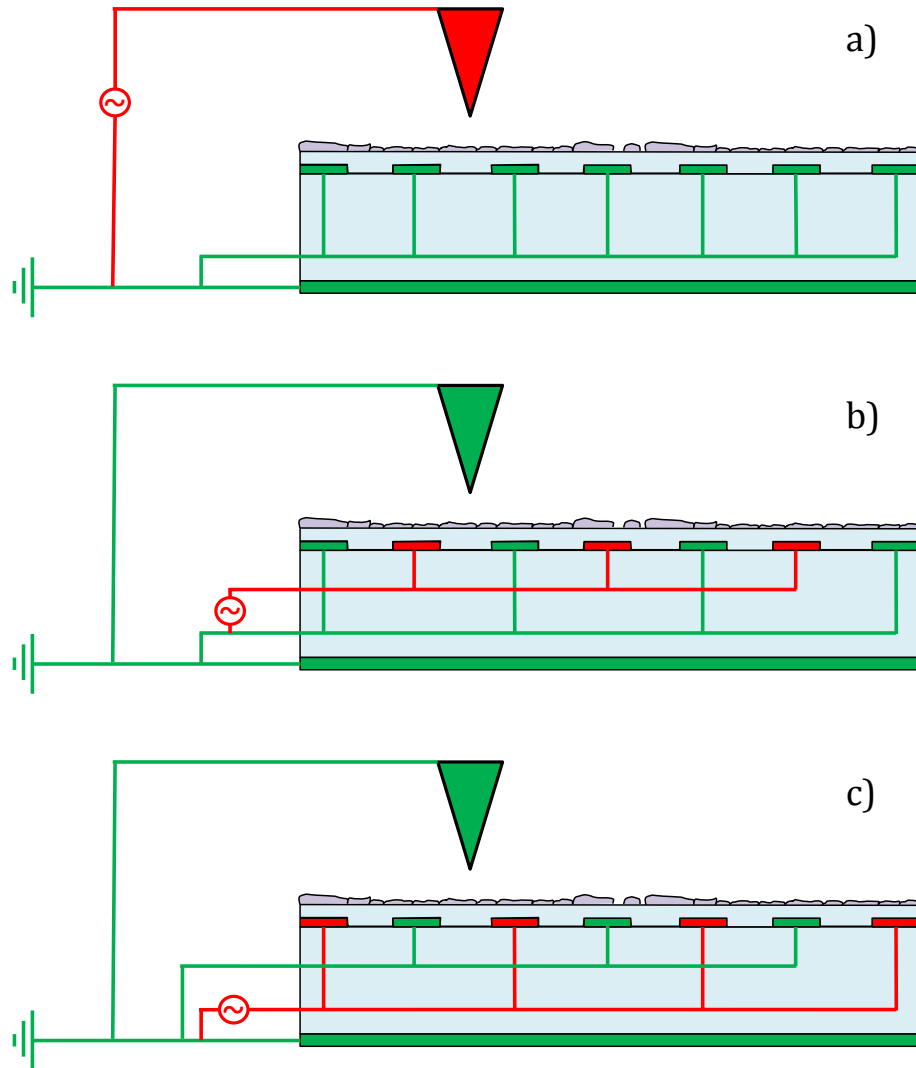


**Figure 3.7.** AC excitation modes: a) through the cantilever, IDA electrodes on the same ground. b) through one set of arrays, the other one and the cantilever on the same ground. c) same as in b), only with the excitation on the opposite set of arrays.



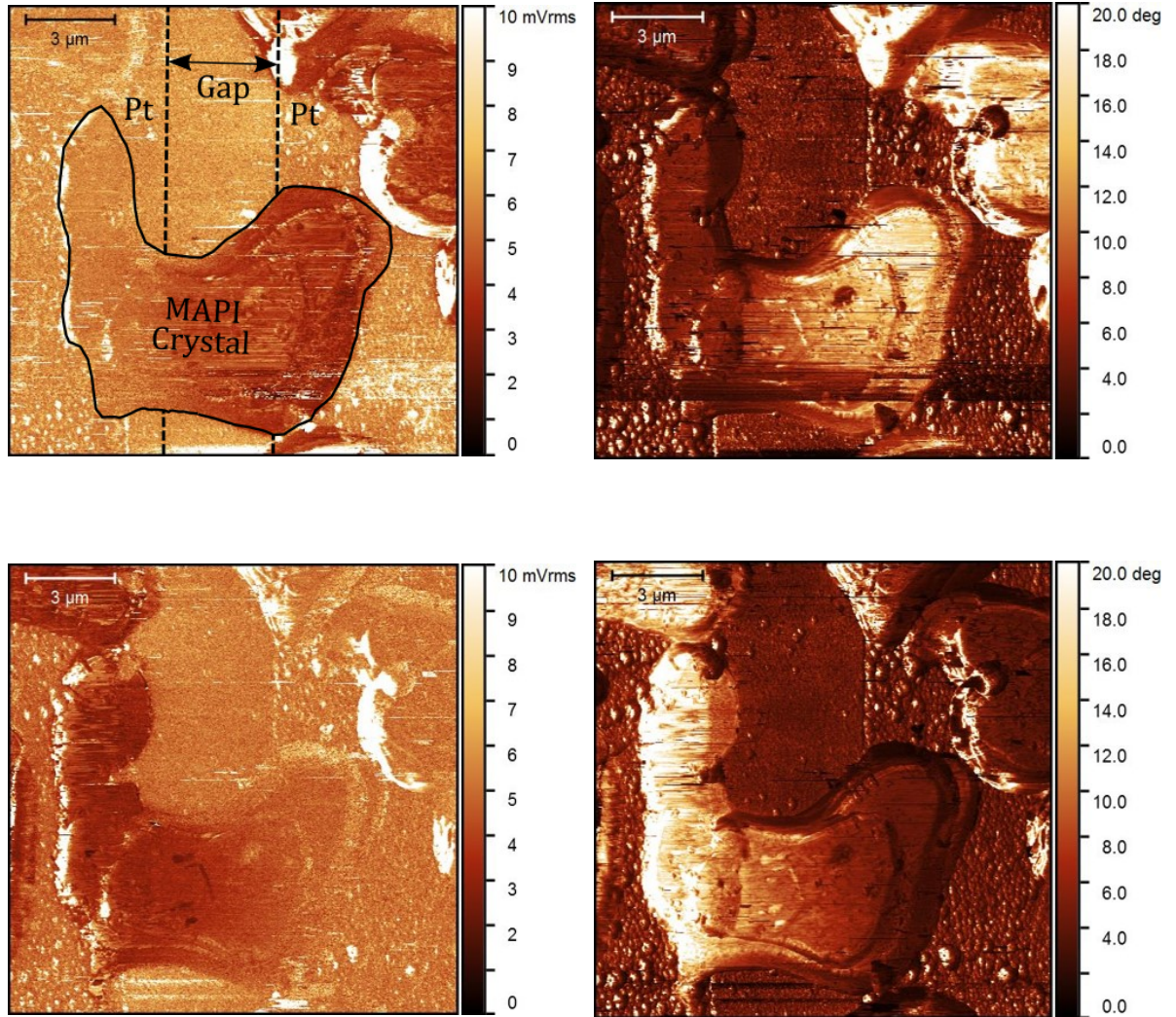


**Figure 3.8.** PFM images: Top row is the amplitude and phase signal with the configuration of figure 3.7 b), bottom row with inverted polarity (figure 3.7 c)). The top left picture indicates the position of the electrode gap, the platinum electrodes (Pt) and the MAPI crystal.

### 3.4 Domain Characterization

In the following sections, several experiments are conducted, in order to characterize the obtained domain patterns. This means, that the results from these experiments clarify, which domain patterns are present, and how the unit cell orientation in the domains looks like.

The first experiment compares the vertical and the lateral PFM response of the same grain. This way, out of plane and in plane orientations can be distinguished from one another.

The following hysteresis measurement checks, if an electrical out of plane polarization component is present. This is a criterion for ferroelectricity.

The last experiment combines the PFM measurement with an LDV laser. This way, possible cantilever dynamics for the out of plane response can be excluded. As a result, one can conclude, if the measured domain pattern actually has a real piezoelectric out of plane component.

#### 3.4.1 Vertical and Lateral Response

The grain in the following pictures is grown on a FTO substrate, whose layer architecture is shown in figure 3.1. This single grain shape preferably occurs close to the gold electrodes on the substrate, captured in figure A.2 in the appendix. Unfortunately, the grains did not crystallize like this in the designated gold gap, so that switching experiments could not be performed in this case. Instead, very clean PFM images are obtained here and the lateral signal can be compared to the vertical one (figures 3.9 and 3.10, both scanned in a  $90^\circ$  cantilever scan mode).

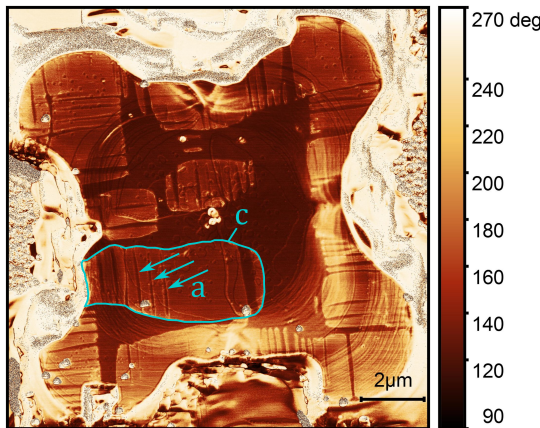


**Figure 3.9.** Vertical PFM,  $90^\circ$

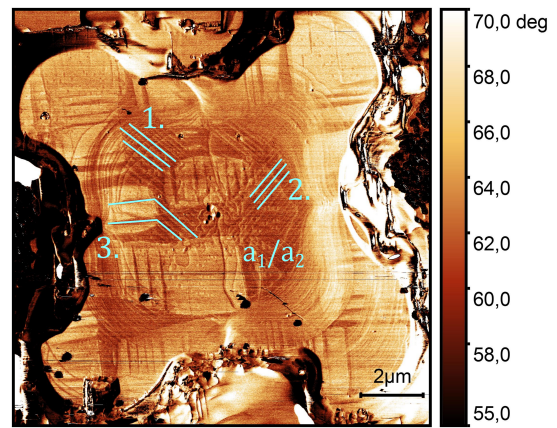


**Figure 3.10.** Lateral PFM,  $90^\circ$

In the vertical PFM image, the phase contrast of almost  $180^\circ$  comes from two different domains, a dark one in the middle and a brighter one, which is partially permeated in lens shaped stripes by the former one (see marks).

### III. Experiment & Results

---

In earlier measurements on perovskites with the same phase transition symmetry as MAPI, namely  $\text{PbTiO}_3$  and PZT, this kind of domain structure has been observed as well [LCLB01][RPW<sup>+</sup>02]. As it is evaluated there, the domain pattern in this case can similarly be assigned to the  $a/c$ -pattern (2.10).

The lateral measurement shows a phase contrast of around  $15^\circ$ , therefore it is much lower than the vertical one. This is due to the weaker contact resonance enhancement in the lateral mode. Nevertheless, with the correct adjustment, an additional stripe pattern with alternating and equidistant bright and dark phase signal becomes visible (indicated with the marks). There are mainly two stripe orientations, which respectively point towards opposing corners of the grain (1. and 2.). At intersections, they cross in a  $90^\circ$  angle. From XRD diffraction measurements on these domains it is confirmed, that mainly the (110) crystal plane is parallel to the surface [HBB<sup>+</sup>16]. Since the domains only appear in the lateral PFM measurement, it means that they only have an in-plane polarization component. With these collected observations, these domains can be assigned to the  $a_1/a_2$ -pattern (2.10). This interpretation is also consistent with the one in the vertical measurement, since the stripes from the  $a_1/a_2$ -pattern merge into the lens shaped  $a$ -stripes from the  $a/c$ -pattern (see mark number 3.). With these assignments one can conclude, that the lateral PFM measurement clearly shows a coexistence of  $a/c$ - and  $a_1/a_2$ -domains.

In previous measurements of this kind, this coexistence of  $a_1/a_2$ - and  $a/c$ -patterns has rarely been observed [TCF10]. An explanation for this unforeseen appearance could be the grain's location close to the gold electrodes: During the evaporation process, it is possible that some gold atoms are scattered beyond the mask's edges onto the  $\text{SiO}_2$  surface. When a grain crystallizes above this spot, the gold atoms can influence the surface tensions and therefore change the growing process of the crystals. This may lead to a configuration, where both of the pattern variants are allowed and lead to the lowest strain energy of the system.

One more interesting aspect is the aforementioned  $a_1/a_2$ -stripe orientation towards the grain corners. This is a hint on a possible correlation with the crystal growth direction, since it preferably happens along the corners (or the edges, depending on the crystal) due to the most rapid heat release at these positions.



### 3.4.2 Hysteresis Measurement

Hysteresis curves are a hint towards ferroelectric behavior, because they can result from remanent polarization in the material, when applying an electric field. In this section, the ferroelectric character of MAPI is revised, by investigating if the crystals show an electrical hysteresis curve. Therefore, a pulsed triangular voltage is applied between the cantilever tip on top of the crystal and the back electrode, as it is shown in figure 3.11. In this function, a series of increasing and decreasing voltages is applied

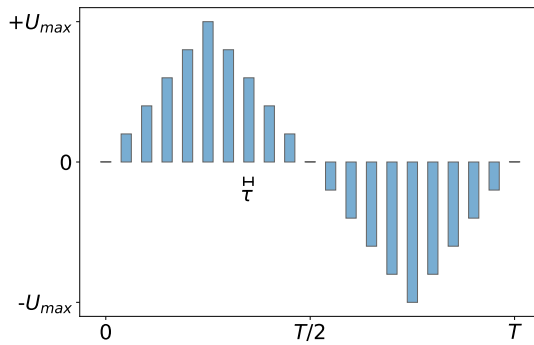


**Figure 3.11** Pulsed triangular voltage: In this experiment, the following parameters for this function are engaged: Maximal voltage  $U_{max} = 72$  V, Period  $T = 0,417$  s ( $f = 2,4$  Hz), Pulse duration  $\tau = 3$  ms, Cycles  $n = 15$ .

to the system. In the gaps in between, the voltage is turned off and the response of the crystal is measured. This leads to a data set of amplitude and phase signal similar to the PFM method, only with an applied pulsed triangular function instead of a sinus and only at one point. With this dataset, one can calculate a hysteresis curve for the phase and for the amplitude signal.

The aim of this experiment is to examine, if the hysteresis curves show a different behavior, when the measurement is taken on top of different domain patterns of the crystal. The PFM image and the resulting phase hysteresis curves are shown in figure 3.12, the corresponding amplitude “butterfly” curves can be taken from A.4.

As a fitting model, the so called “Langevin function” is considered, which has the form

$$\mathcal{L}(x) = \coth(x) - \frac{1}{x}. \quad (3.1)$$

This function is often used to describe resistivity, magnetism and orientational polarization, and is thus a natural choice for this case. Introducing four different degrees of freedom for the fitting procedure, the function changes to

$$\mathcal{L}(x) = a \cdot \left( \coth(b \cdot x - c) - \frac{1}{b \cdot x - c} \right) + d. \quad (3.2)$$

Taking two Langevin fit functions for one hysteresis and calculating the difference in the x-offset times 1/2, one gets the so called “coercive voltage” ( $U_C$ ), a quantity for withstanding an electric field without getting depolarized.

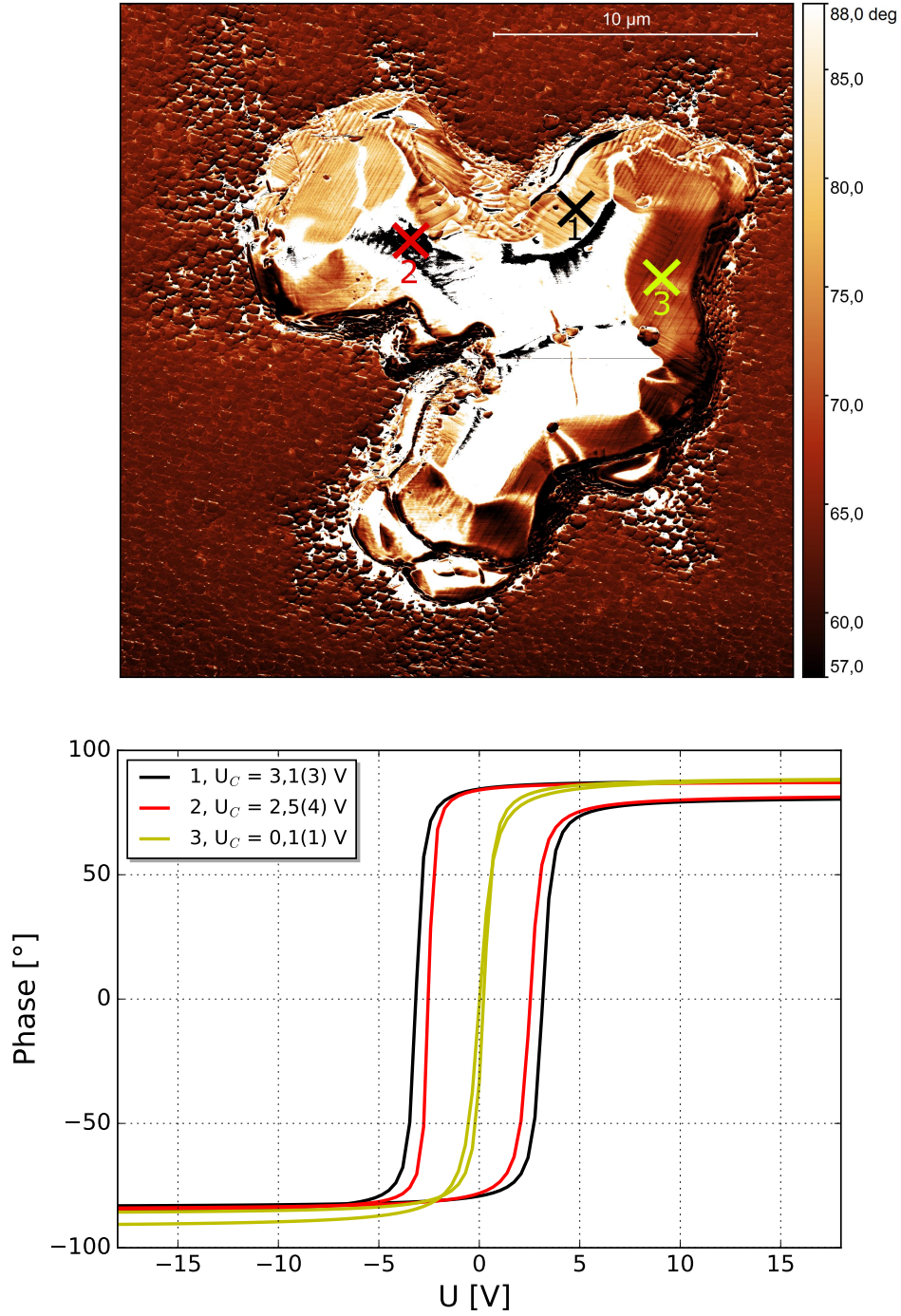


**Figure 3.12.** *Top:* PFM phase image with three different tip positions for the vertical hysteresis measurement. *Bottom:* Corresponding hysteresis curves with the associated coercive voltages  $U_C$  (abscissa cross points). The fitting model is the Langevin function, the data points are omitted, and the x- and y- offsets of all functions are shifted to zero for better clarity and comparability. Full data sets, butterfly curves and further details can be found in the appendix (A.3 & A.4).

Position number 1 shows the highest value of  $U_C$ , number 2 has a slightly lower value and at 3 it is almost zero. The difference between 2 and 3 can be explained with a possibly different pattern: Point 3 is in an ordinary  $a_1/a_2$ -pattern, and therefore has no out of plane polarization component, which could contribute to a hysteresis curve. On the other hand, point 2 in the grain plateau could be in a  $a/c$ -pattern, where the  $c$ -domain is completely out of plane and therefore interacts with the applied voltage. Point 1 obviously has the same pattern as point 3, but as opposed, it has a non zero value for  $U_C$ . This could be attributed to it's location on the grain slope: Due to the tilting of the surface, the polarization vector changes it's orientation as well and gets a component pointing out of the plane.

One has to be careful with these interpretations though, since there are other mechanisms, which can contribute to a hysteresis as well, and therefore be a reason for misinterpretations: One of them, which is already mentioned in section 2.5.3, is *electromechanical strain*. Besides potentially influencing the PFM signal, it can as well create electrical fields through ion redistribution, which then act as polarization vector. In fact, hysteresis curves have been observed on materials, where there is no ferroelectric behavior expected whatsoever [Sco07]. For this reason, ferroelectricity can not be certainly concluded from this experiment.

In order to really confirm ferroelectricity in MAPI in future experiments, one can check the frequency dependence in more detail, with which the pulsed triangular voltage is applied: Ionic fluctuations happen in a much higher frequency regime than ferroelectric polarization switching. So if there are hysteresis curves in the low frequency regime as well, the ionic movements can be excluded with a higher certainty.

In order to investigate the  $U_C$ -dependence on the in plane  $a_1/a_2$ -domain orientation, the electrical excitation has to be shifted in plane as well. This can be realized with lateral electrodes, as it is shown in 3.2, where the triangular voltage can be applied between the cantilever and one of the electrodes. This way, the proposition of the polarizing vector being completely in plane [HBB<sup>+</sup>16] can be further inspected.

### 3.4.3 Laser Doppler Vibrometer

The measurements presented in the following section were taken in a combined setup of a commercial Cypher AFM (Asylum Research, Santa Barbara, CA) together with an integrated quantitative Laser Doppler vibrometer (LDV) system (Polytec GmbH, Waldbronn, Germany), all arranged in the Oak Ridge National Laboratory (TN, USA). With this method, possible cantilever dynamics, which are explained in section 2.5.2, can be excluded from the real piezoelectric out of plane response. The main purpose of this experiment is to exclude a possible out of plane polarization component from the  $a_1/a_2$ -domain pattern.

As it is explained in section 2.5.4, a LDV measures the velocity of a vibrating object. In this case, the vibrating object is the cantilever, which has an angular motion instead of a linear one. Therefore the oscillation amplitude  $x$  has to be recalculated via

$$x = v/2\pi f, \quad (3.3)$$

where  $v$  represents the LDV velocity (a.k.a. the “sensitivity setting”,  $[v] = \text{mm/s/V}$ ) and  $f$  is the cantilever drive frequency. With this quantity, the maximal displacement per applied voltage can be visualized in the PFM phase images.

In this experiment, the PFM images of two laser positions are compared to one another: The first one has the laser spot purposely removed from the position directly above the cantilever tip. This way, possible cantilever dynamics are included in the measurements. The second setting is with the LDV laser placed just directly over the cantilever tip, in order to only have real vertical displacement of the cantilever. The results are shown in figure 3.13.

Even if the images are not as clean as the previous ones (probably due to the ambient environment of the Cypher AFM), the most noticeable aspect is, that the contrast almost vanished after the LDV laser spot was moved directly over the cantilever tip. Resulting from equation 3.3, the background noise level for the vertical cantilever displacement is  $5 \text{ pm/V}$ . Since the average amplitude of  $1,7 \text{ pm/V}$  is lower than this background level, one can conclude that there is no amplitude contrast detectable in this measurement. The small remaining contrast in the amplitude as well as in the phase images could possibly come from a non perfect positioning of the LDV laser spot above the cantilever tip.

As a result from this experiment it can be concluded, that the observed domains can not be assigned to the  $a/c$ -pattern, due to the missing out of plane component. Therefore it must be the  $a_1/a_2$ -pattern, with a complete in plane polarization orientation.



### 3.4. Domain Characterization

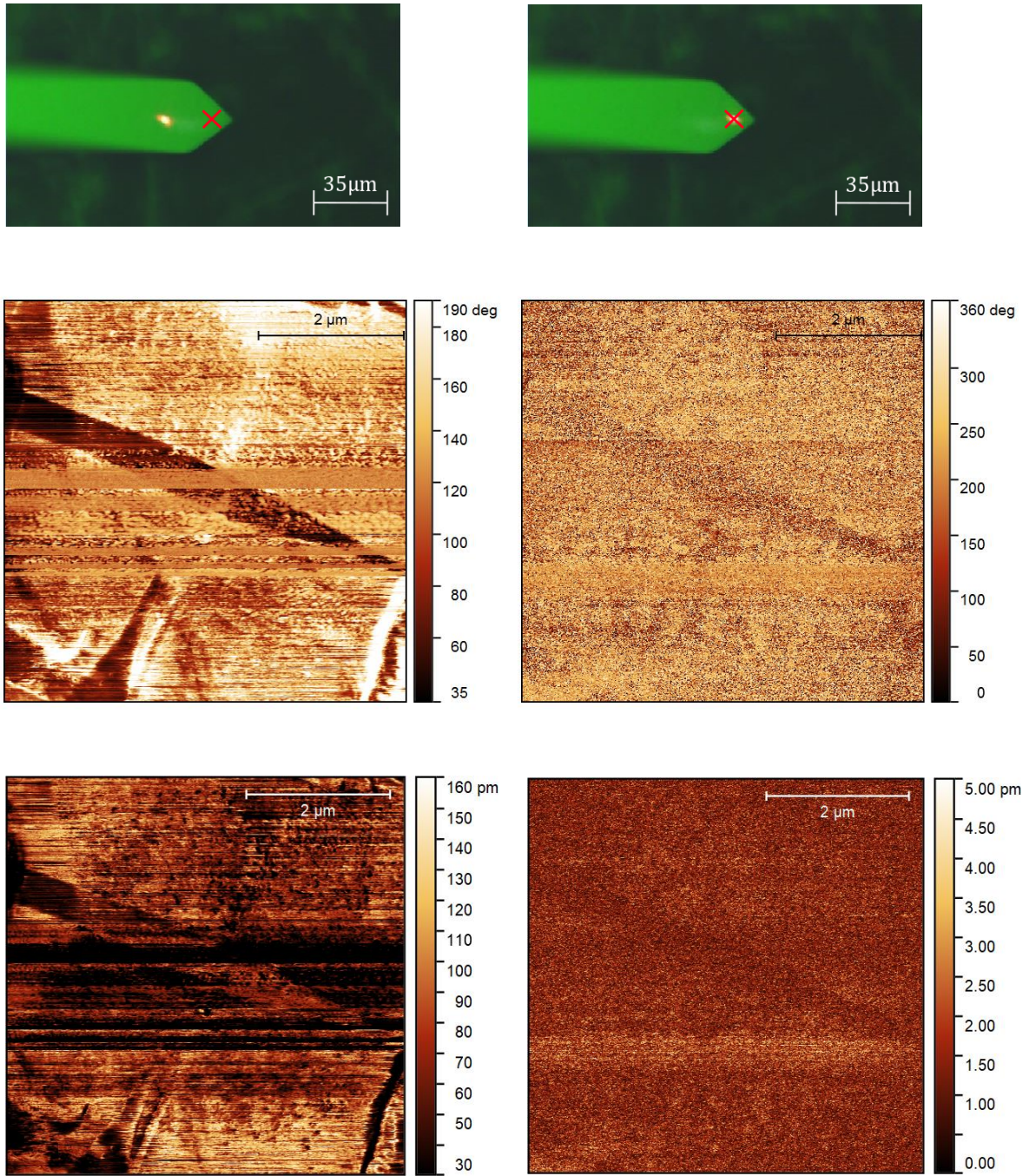


**Figure 3.13.** Measurements with the Laser Doppler Vibrometer. Left column: Phase and amplitude signals with the laser spot removed from the position above the tip. Right column: Same measurement with the laser just above the tip.

## 3.5 Domain Manipulation

In this section the manipulation possibilities of the ferroelastic twin domains are presented. These include mechanical strain, temperature and an electric field.

### 3.5.1 Mechanical Strain

The crystal in this experiment was grown on a simple glass substrate. After obtaining the first PFM image, the sample was accidentally scratched mechanically with a needle. After that, the same area was scanned again, resulting in the images in figure 3.14.

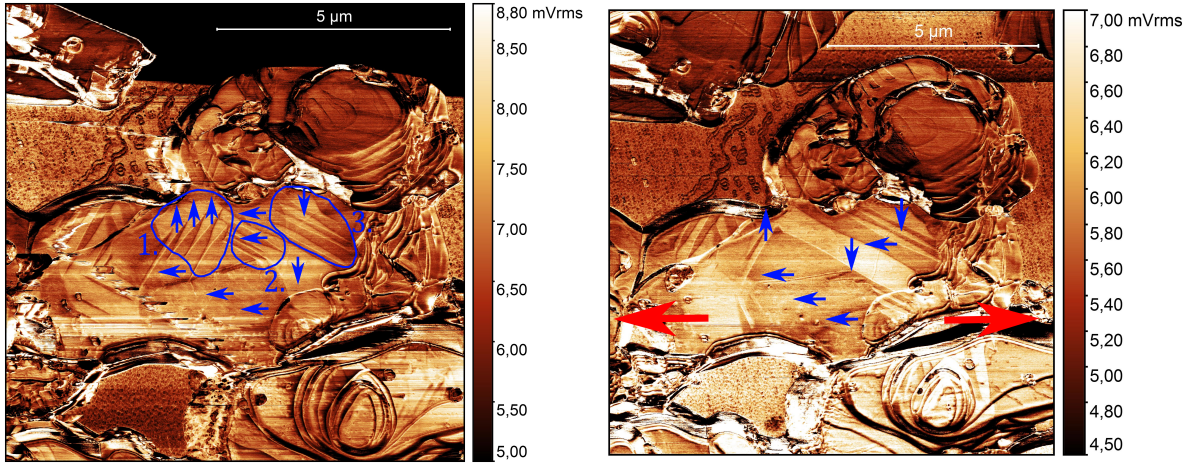


**Figure 3.14.** Amplitude images of MAPI crystals before (left) and after (right) applying an arbitrary strain onto an area left of the displayed image section.

The domain pattern has changed due to the deformed substrate surface. The mechanical pressure on the needle created an extensive stress vector, which stretched the grain horizontally. In figure 3.14, this is indicated with red arrows.

The most significant changes after the mechanical strain are marked with blue circles: In region 1 and 3, the bright tapered domains disappeared at cost of the darker one's, while the bright domains in region 2 merged to one large area.

The explanation for this behavior is the preferred alignment of the unit cell's  $c$ -axis with the extensive stress vector. The direction of this axis is indicated with blue arrows, in accordance with the  $a_1/a_2$ -domain pattern. Due to a lowering of the total strain energy in the system, the total number of stripes with an orientation perpendicular to the stress vector is reduced.

In general, the tapered domains are energetically unfavorable, due to the high surface energy of the domain walls. With an external vibration, as it happened due to the scratching, this energy can be minimized by reducing the total number of such domains. This experiment confirms the mechanical and respectively the ferroelastic behavior of MAPI crystals.



### 3.5.2 Slow vs. Rapid Cooling

In the following experiment, the influence of different cooling rates on the domain pattern was explored. This approach is inspired by the malleablizing process of glass, which is used to reduce mechanical strain during the manufacturing. If the glass is cooled down too fast, it cracks up. The rapid cooling results in high temperature gradients, which lets certain micro structure domains cool down faster than their neighboring ones. With such inhomogeneities, it is energetically more favorable for the glass to form small fissures, which can also become macroscopic, depending on the cooling rate.

When this is now projected to the elastic component of the MAPI crystals, it is likely that this material can be influenced similarly: When it is cooled down fast, the stress during the cooling process is higher. Therefore, more domain patterns (“fissure”) than usual show up, in order to reduce the total strain energy of the system (as described in section 2.3.2). The faster the cooling process, the less time does the system have to rearrange it’s crystal structure continuously. Therefore, this process can be seen as a “freezing” of a non-equilibrium configuration.

In this experiment, a FTO sample (3.1) was placed on the CoolerHeater stage (Asylum Research), where parameters as the set point temperature and the heating-/cooling rate can be specified. For the high rates, an additional cycle with cooling fluid was installed to avoid an overheating of the Peltier elements. The measurement procedure was the following: First the sample was heated up to 65°C, then it was cooled down with a defined rate  $\dot{T}$ , and finally a PFM image of the same area is recorded. Figures 3.15 and 3.16 show the images for cooling rates of  $\dot{T}_1 = -2^\circ\text{C/s}$  and  $\dot{T}_2 = -50^\circ\text{C/s}$ .

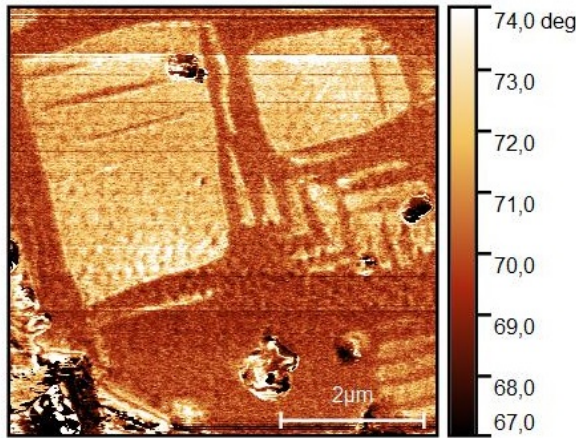


Figure 3.15.  $\dot{T}_1 = -2^\circ\text{C/s}$

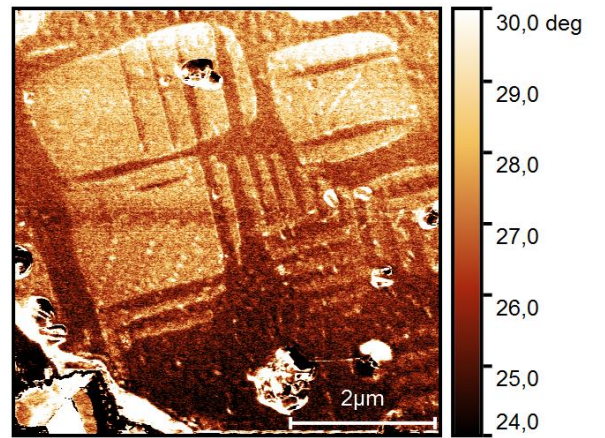


Figure 3.16.  $\dot{T}_2 = -50^\circ\text{C/s}$

Compared to previous experiments, the domain structure in these images resemble the *a/c*-pattern. As expected, the rapid cooling image shows more domain structures than the slow cooling one. This is consistent with the assumptions from above and thus with the mechanical fissure character of the domains.

### III. Experiment & Results

---

One has to consider though, that the sample is previously heated up to a temperature, which is higher than  $T_C$ . So even though the image matches with the model, the structure could also partially come from an arbitrary reorientation of the unit cells in the cubic phase. Furthermore, the examined area of interest is only around  $6\text{ }\mu\text{m}$  x  $6\text{ }\mu\text{m}$  large. In order to get a better statistical evidence of this effect, one has to observe the change in structure on a larger area.

A different explanation for this effect is the mismatch of the grain with the substrate surface, as it is mentioned in section 2.3.2. When varying the cooling rate, the different thermal expansion coefficients of the glass and the MAPI crystals play a role: As the whole system is cooled down with a certain rate, the two substances acclimatize to this change with two different velocities. This leads to mismatches on the contact area between the glass and the MAPI crystals. In order to reduce the mechanical strain energy, which results from this mismatch, the characteristic domain pattern is formed. When the cooling rate is faster, the acclimatization difference is correspondingly higher. This leads to more mismatches on the contact area, a higher mechanical strain and therefore to more domains.



### 3.5.3 Electrical Switching

In this section, the domain orientation was switched, by the application of a lateral electric field. As a result from section 3.3, the IDA sample is an appropriate choice. This experiment runs in three different steps, which are now further explained:

*First*, a lateral PFM measurement was executed on the prepared IDA sample. The electric field lines during this step are shown in figure 3.17. The IDA's and the aluminum layer on the bottom of the substrate were grounded on the same potential, the latter one acts as back electrode which is needed for the PFM measurement.

*Second*, the cantilever was lifted from the surface and the Asylum heating stage under the sample was heated up to  $\sim 50^\circ\text{C}$ , as a result from the temperature calibration in section 3.2. When the temperature equilibrated to this set point, a voltage of 50 V was applied between the IDA's for 3 h, while the back electrode was grounded. This voltage was chosen, because it is just below the avalanche voltage of this setup. The electric field line distribution in this moment is shown in figure 3.18.

*Third*, the procedure from step one was repeated to obtain the new domain structure.

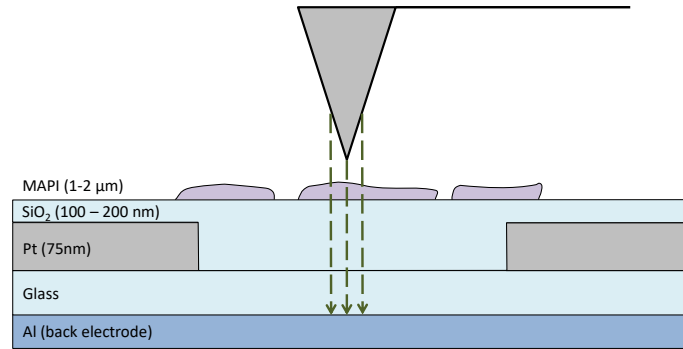


**Figure 3.17.** Electric field lines during PFM measurement.

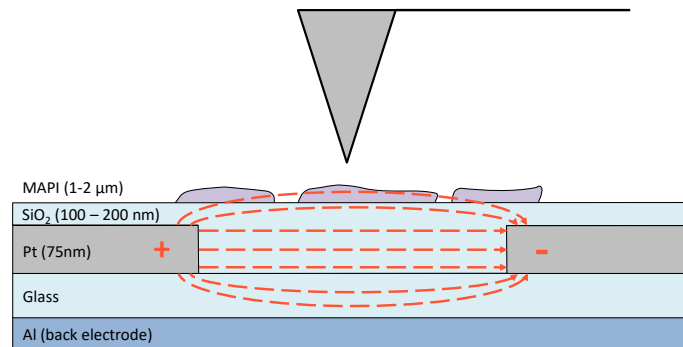


**Figure 3.18.** Electric field lines during horizontal electrical switching.

### III. Experiment & Results

In the following, three different areas are presented, which show a change in the domain structure after the application of the electric field. The corresponding lateral PFM phase images are shown in figure 3.19 to 3.21, whereas the left pictures always show the area before, and the right ones show the same area after the electric field.

The first case begins with a grain, which does not have any domain structure whatsoever (figure 3.19). It is located just above the intersection of a platinum electrode and a gap. This border is marked with a red dashed line. After the voltage application, a domain structure parallel to the border appeared.

Due to the applied voltage, the polarization vector in the tetragonal unit cell of MAPI tends to align with the electric field vector, since this configuration is energetically favorable. Therefore it makes sense, to assign the polarization orientations in the domains as it is indicated by the small blue arrows in the box. As a result, the net polarization vector of the domains, indicated as a large blue arrow, is aligned with the electric field vector, shown in red. The arrangement of the small blue arrows belongs to the  $a_1/a_2$ -domain pattern, which has already been observed in figure 3.10 from section 3.4.1.

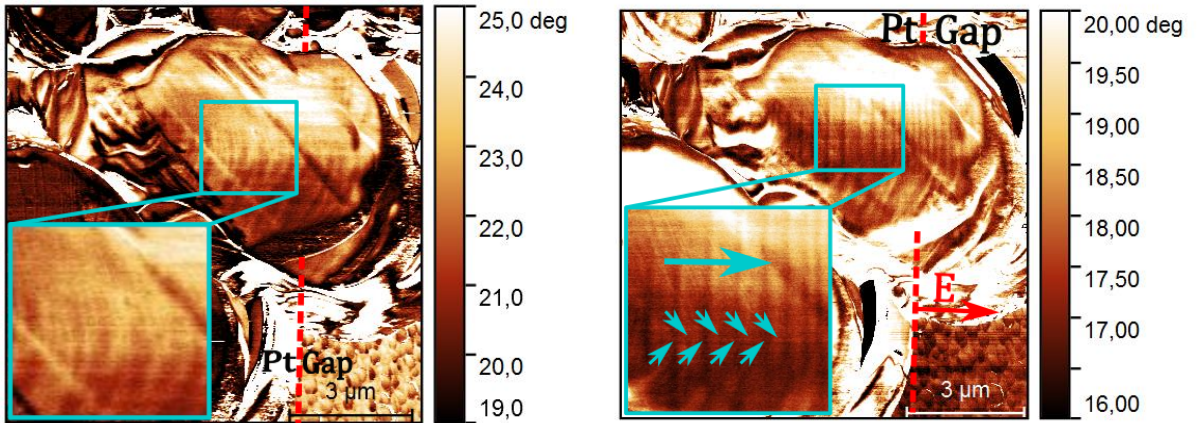


**Figure 3.19.** First switching event: The appearance of new domains. Lateral PFM phase images before (left) and after (right) the application of the electrical field.  $T = 50^\circ\text{C}$ ,  $U = 50\text{ V}$ ,  $t = 3\text{ h}$ . The small blue arrows indicate the polarization orientation in the domains. The large blue arrow represents the net polarization direction. The red dotted line shows the border between platinum electrode below the crystal (Pt) and the gap. The red arrow points in the direction of the electric field.

The second case is a grain, where parts of it already show the  $a_1/a_2$ -pattern (figure 3.20). Nevertheless, a large area still shows no domains at all (see blue box). After the electric field, the empty area adapted to the already existing pattern. As a result, the whole area of the inspected grain is covered. The explanation from the first case also holds for this one. It is remarkable though, that the net polarization vector is not perfectly aligned with the electric field. This can be explained with the contact area between the grain and the substrate surface: When the crystal starts to grow on the surface, the first layer of MAPI determines the growth direction of the remaining crystal. When an electric field is applied after the growing process is finished, the domain reorientation is always a compromise: On one hand, the net polarization vector has to be aligned with the electric field, on the other hand, the new domain structure has to be consistent with the already existent one. An application of an electric field during the growth process could possibly influence the structure from the beginning.

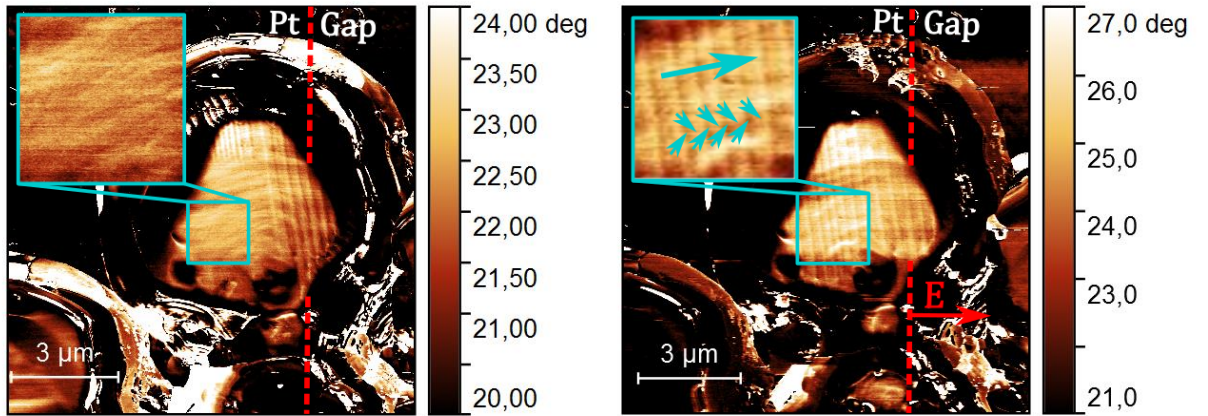


**Figure 3.20.** Second switching event: Adaptation of the existing domain pattern.

### III. Experiment & Results

The third case starts as well with an already existing  $a_1/a_2$ -pattern (figure 3.21). After the application of the electric field, a continuous  $\sim 45^\circ$  kink appeared in the domain pattern, which follows a track right along the electrode edge. A formation like this is energetically strongly unfavorable. Since the domain change is only located just at the electrode edge, the electric field is the only explanation for this observed domain switch, since it begins and ends at the electrode edges as well (see figure 3.18). The  $45^\circ$  angle between the  $a_1/a_2$ -pattern and the new one indicates, that the latter one is an  $a/c$ -pattern, as it has been already observed in figure 3.10. The appearance of this out of plane component is perfectly in agreement with the electric field at the edge, since the latter also has a vertical component, as it is sketched in figure 3.18 at the electrode edges.

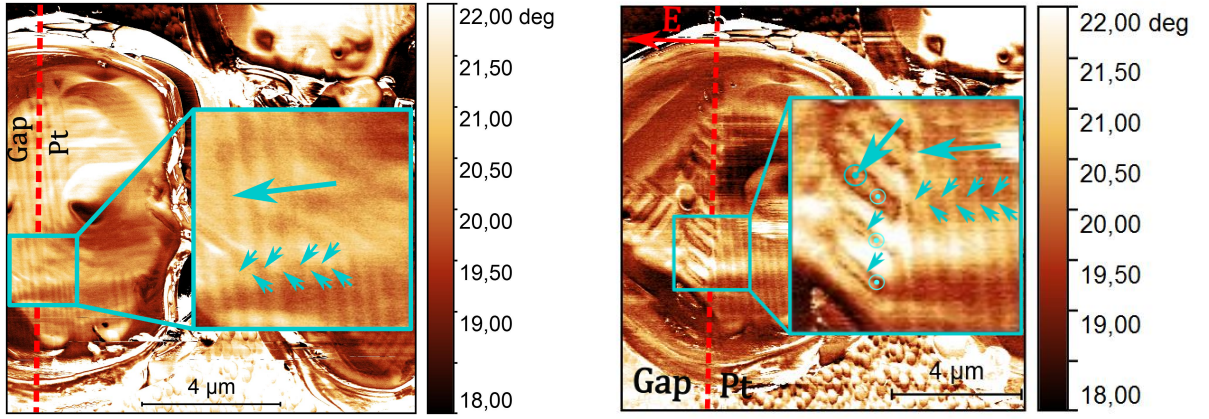


**Figure 3.21.** Third switching event: Reorientation of the domains.

As a result of all switching events, either the  $a_1/a_2$ - or the  $a/c$ -pattern can appear, in order to reduce the total energy of the system. This depends individually on the confinement with the remaining crystal structure of the grain. Either way, these experiments have clearly shown, that ferroelastic domain patterns in MAPI can be shaped or switched by an electric field. This means, that a polarization vector must be present in the domains, which makes MAPI a ferroelectric material.

## IV. Conclusion & Outlook

In this thesis, the behavior of MAPI crystals were inspected, in order to gain additional knowledge about the crystal structure within the domains and about the ferroelectric character of the material.

The comparison of the **lateral** and the **vertical PFM** response confirmed the assignment of the equidistant domains to the  $a_1/a_2$ -pattern. Furthermore, a possibly different structure was observed, which is attributed to the  $a/c$ -pattern, based on earlier measurements and arguments for minimal energy. In order to confirm this assignment, further measurements like X-ray diffraction on these kind of crystals is recommended.

The appearance of a **hysteresis loop** in the following experiment seemed promising for a ferroelectric behavior. Nevertheless, this appearance alone does not allow a clear assignment to ferroelectricity, since there are still several other effects, which could lead to a similar result. For a clearer exclusion from ion migration, the frequency dependency of the AC-voltage has to be inspected in more detail. Furthermore, a Kelvin Probe Force Microscopy measurement can possibly detect this effect as well. An application of lateral electric fields is also recommendable, in order to check on in plane hysteresis loops.

With the **Laser Doppler Vibrometer** measurement, a pure in plane polarization of the  $a_1/a_2$ -domain pattern was confirmed. For future experiments it is recommendable, to conduct this experiment on a sample with coexisting  $a_1/a_2$ - and  $a/c$ -domains, in order to observe the effect of the Laser Doppler Vibrometer on both of the domain patterns.

The **mechanical stress** experiment confirmed the ferroelastic character of the domains, since an alignment of the  $c$ -axis along an applied stress orientation could be observed.

The comparison of **slow and rapid cooling** rates confirms the model, that the domain formation also correlates with the mismatches of the crystals and the substrate within the contact area. In order to further examine this behavior, these measurements can be conducted on substrates with predefined structures, such as nanopillar arrays. This way, possible correlations with the surface can be observed.

As a final result, the positive outcome of the **electrical switching** experiment confirms ferroelectricity in MAPI.



## A. Appendix

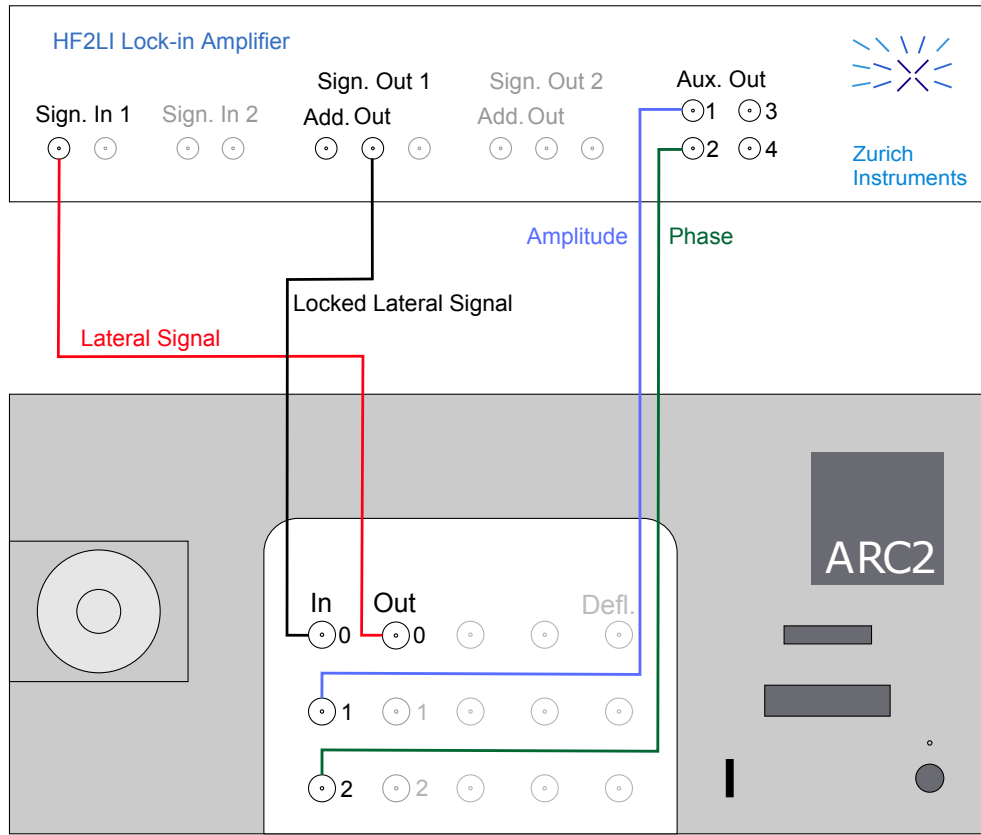


**Figure A.1.** Circuit diagram of the ARC2/Zurich Lock-in setup for lateral PFM-mode measurements. For vertical PFM-mode, the lateral signal is replaced with the deflection signal. The figure is adapted from [AHB<sup>+</sup>18].



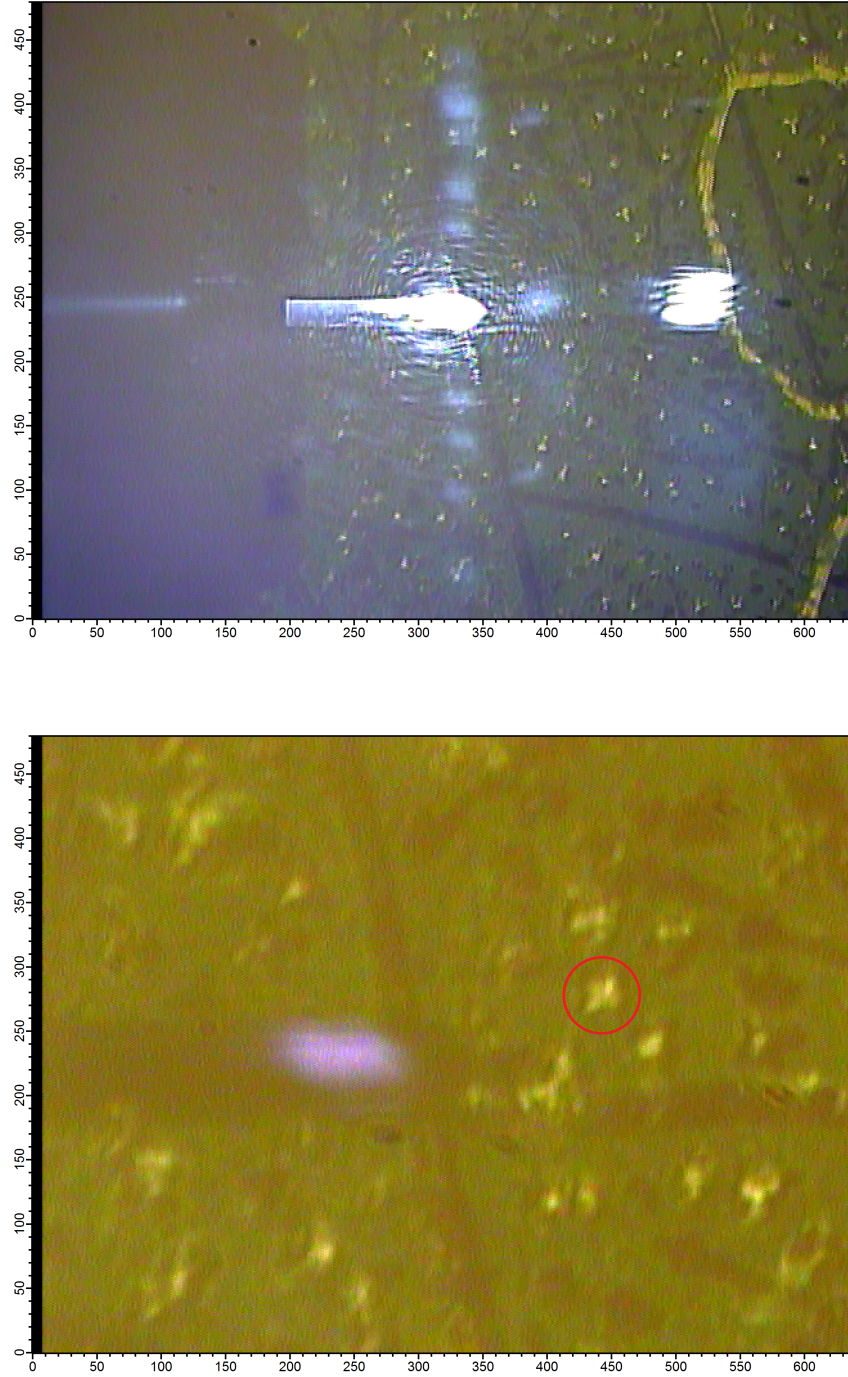


**Figure A.2.** Optical microscope images of the grain in figure 3.9 and 3.10. Top: Other single crystals are well visible as bright spots due to the flat surface and the resulting good reflectivity. The laser spot on the cantilever, a reflection further right and a scratched mark on the right border are visible as well. The gold electrode is not in this area, but close to the top horizontal line of the image. Bottom: Zoomed picture with a red circle around the investigated grain.

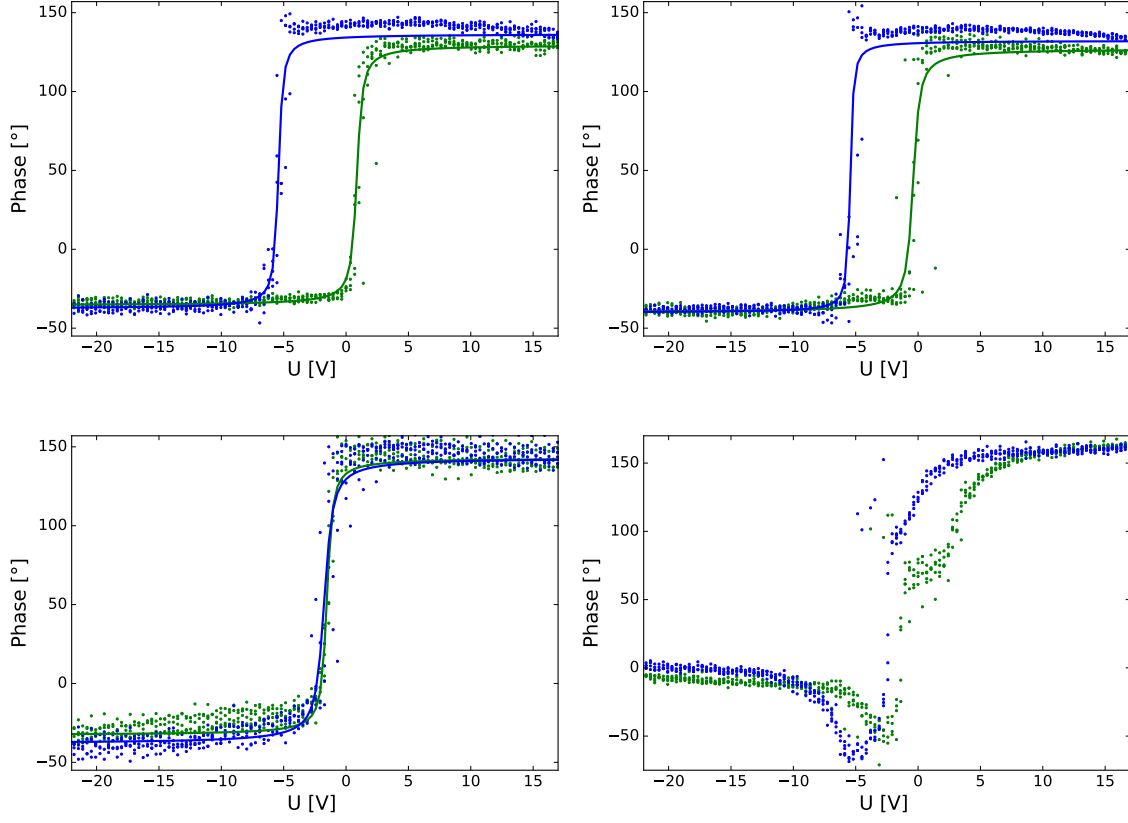


**Figure A.3.** Hysteresis data points and fit curves. The blue line represents increasing voltages and the green one decreasing voltages, with a total of 15 repetitions. From top left to bottom right, measurements on positions 1 to 3 are displayed. The graph on the bottom right position shows a reference measurement outside of the grain on the SiO<sub>2</sub> substrate surface.

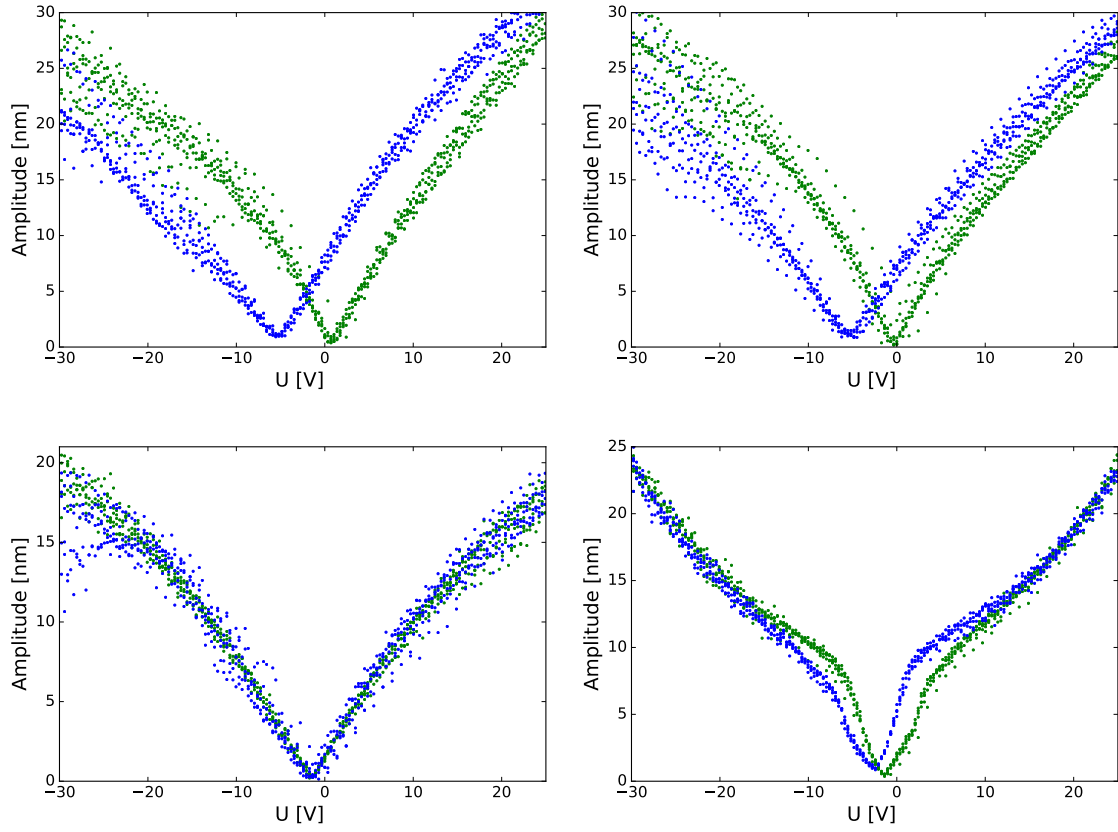


**Figure A.4.** Butterfly data points. The measurement cycles and the order of the measurements correspond to the graphs and description in figure A.3.



## B. Bibliography

- [AHB<sup>+</sup>18] Amelie Axt, Ilka M Hermes, Victor W Bergmann, Niklas Tausendpfund, and Stefan AL Weber.  
Know your full potential: Quantitative kelvin probe force microscopy on nanoscale electrical devices.  
*Beilstein Journal of Nanotechnology*, 9(1):1809–1819, 2018.
- [Aiz70] Kêitsiro Aizu.  
Possible species of ferromagnetic, ferroelectric, and ferroelastic crystals.  
*Physical Review B*, 2(3):754, 1970.
- [B<sup>+</sup>03] Kaushik Bhattacharya et al.  
*Microstructure of martensite: why it forms and how it gives rise to the shape-memory effect*, volume 2.  
Oxford University Press, 2003.
- [Bee14] Jürgen Beetz.  
 *$E = mc^2$ : Physik für Höhlenmenschen*.  
Springer-Verlag, 2014.
- [BFS<sup>+</sup>15] Federico Brivio, Jarvist Frost, Jonathan Skelton, Adam Jackson, Oliver Weber, Mark T. Weller, Alejandro Goñi, Aurelien Leguy, Piers Barnes, and Aron Walsh.  
Lattice dynamics and vibrational spectra of the orthorhombic, tetragonal and cubic phases of methylammonium lead iodide.  
*Physical Review B*, 92:144308, 10 2015.
- [BQG86] G. Binnig, C. F. Quate, and Ch. Gerber.  
Atomic force microscope.  
*Phys. Rev. Lett.*, 56:930–933, Mar 1986.
- [Ene18] Energy watch group.  
Fossil fuel peak in the 2020s.  
<http://energywatchgroup.org/energy-watch-group-newsletter-september-2018>,  
September 2018.
- [FBW14] Jarvist M Frost, Keith T Butler, and Aron Walsh.  
Molecular ferroelectric contributions to anomalous hysteresis in hybrid perovskite solar cells.  
*Apl Materials*, 2(8):081506, 2014.
- [FXS<sup>+</sup>15] Zhen Fan, Juanxiu Xiao, Kuan Sun, Lei Chen, Yating Hu, Jianyong Ouyang, Khuong P Ong, Kaiyang Zeng, and John Wang.  
Ferroelectricity of  $\text{CH}_3\text{NH}_3\text{PbI}_3$  perovskite.  
*The journal of physical chemistry letters*, 6(7):1155–1161, 2015.
- [GM71] H Gränicher and KA Müller.

- On the nature of phase transitions and nomenclature.  
*Materials Research Bulletin*, 6(10):977–987, 1971.
- [HBB<sup>+</sup>16] Ilka M Hermes, Simon A Bretschneider, Victor W Bergmann, Dan Li, Alexander Klasen, Julian Mars, Wolfgang Tremel, Frederic Laquai, Hans-Jürgen Butt, Markus Mezger, et al.  
 Ferroelastic fingerprints in methylammonium lead iodide perovskite.  
*The Journal of Physical Chemistry C*, 120(10):5724–5731, 2016.
- [HM55] John A Hooton and Walter J Merz.  
 Etch patterns and ferroelectric domains in BaTiO<sub>3</sub> single crystals.  
*Physical Review*, 98(2):409, 1955.
- [HSA83] Theo Hahn, Uri Shmueli, and JC Wilson Arthur.  
*International tables for crystallography*, volume 1.  
 Reidel Dordrecht, 1983.
- [Int18] International Energy Agency.  
 Total primary energy supply by source.  
<https://www.iea.org/statistics/?country=WORLD&year=2016&category=Energy%20consumption>, September 2018.
- [Kit05] Achim Kittel.  
 Solid state physics.  
 University Lecture, 2005.
- [KRP<sup>+</sup>00] E Kester, U Rabe, L Presmanes, Ph Tailhades, and W Arnold.  
 Measurement of young’s modulus of nanocrystalline ferrites with spinel structures by atomic force acoustic microscopy.  
*Journal of Physics and Chemistry of Solids*, 61(8):1275–1284, 2000.
- [Lan37] Lev Davidovich Landau.  
 On the theory of phase transitions.  
*Ukr. J. Phys.*, 11:19–32, 1937.
- [LCLB01] KS Lee, JH Choi, JeongYong Lee, and S Baik.  
 Domain formation in epitaxial Pb (Zr, Ti) O<sub>3</sub> thin films.  
*Journal of Applied Physics*, 90(8):4095–4102, 2001.
- [LP15] Aleksander Labuda and Roger Proksch.  
 Quantitative measurements of electromechanical response with a combined optical beam and interferometric atomic force microscope.  
*Applied Physics Letters*, 106(25):253103, 2015.
- [MB87] K Alex Müller and J Georg Bednorz.  
 The discovery of a class of high-temperature superconductors.  
*Science*, 237(4819):1133–1139, 1987.
- [Mer54] Walter J Merz.  
 Domain formation and domain wall motions in ferroelectric BaTiO<sub>3</sub> single crystals.  
*Physical Review*, 95(3):690, 1954.

- 
- [Mil39] William Hallows Miller.  
*A Treatise on Crystallography.*  
For J. & JJ Deighton, 1839.
- [Nat19] National Renewable Energy Laboratory.  
Best research-cell efficiency chart.  
<https://www.nrel.gov/pv/cell-efficiency.html>, August 2019.
- [RJA96] U Rabe, K Janser, and Wt Arnold.  
Vibrations of free and surface-coupled atomic force microscope cantilevers: Theory and experiment.  
*Review of scientific instruments*, 67(9):3281–3293, 1996.
- [RPW<sup>+</sup>02] A Roelofs, NA Pertsev, R Waser, F Schlaphof, LM Eng, C Ganpule, V Nagarajan, and R Ramesh.  
Depolarizing-field-mediated 180° switching in ferroelectric thin films with 90° domains.  
*Applied physics letters*, 80(8):1424–1426, 2002.
- [Sch08] Hans Schmid.  
Some symmetry aspects of ferroics and single phase multiferroics.  
*Journal of Physics: Condensed Matter*, 20(43):434201, 2008.
- [Sco07] JF Scott.  
Ferroelectrics go bananas.  
*Journal of Physics: Condensed Matter*, 20(2):021001, 2007.
- [SG17] Phillip Szuromi and Brent Grocholski.  
Natural and engineered perovskites, 2017.
- [SKK17] Daehee Seol, Bora Kim, and Yunseok Kim.  
Non-piezoelectric effects in piezoresponse force microscopy.  
*Current Applied Physics*, 17(5):661–674, 2017.
- [SMD93] Z Surowiak, VM Mukhortov, and VP Dudkevich.  
Phase transitions and domain structure in heteroepitaxial ferroelectric (Ba<sub>1-x</sub>Sr<sub>x</sub>)TiO<sub>3</sub>/(100)MgO and PbTiO<sub>3</sub>/(100)MgO thin films.  
*Ferroelectrics*, 139(1):1–16, 1993.
- [SP94] JS Speck and W Pompe.  
Domain configurations due to multiple misfit relaxation mechanisms in epitaxial ferroelectric thin films. i. theory.  
*Journal of applied physics*, 76(1):466–476, 1994.
- [TCF10] Alexander Kirillovich Tagantsev, L Eric Cross, and Jan Fousek.  
*Domains in ferroic crystals and thin films*, volume 13.  
Springer, 2010.
- [Voi15] Bert Voigtländer.  
*Scanning probe microscopy.*  
Springer, 2015.

## B. Bibliography

---

- [Wad82] Vinod K Wadhawan.  
Ferroelasticity and related properties of crystals.  
*Phase Transitions: A Multinational Journal*, 3(1):3–103, 1982.
- [WHTC<sup>+</sup>18] Stefan AL Weber, Ilka M Hermes, Silver-Hamill Turren-Cruz, Christopher Gort, Victor W Bergmann, Laurent Gilson, Anders Hagfeldt, Michael Graetzel, Wolfgang Tress, and Rüdiger Berger.  
How the formation of interfacial charge causes hysteresis in perovskite solar cells.  
*Energy & Environmental Science*, 11(9):2404–2413, 2018.
- [WW16] Peter Würfel and Uli Würfel.  
*Physics of solar cells: from basic principles to advanced concepts*.  
John Wiley & Sons, 2016.
- [YN98] K Yamanaka and S Nakano.  
Quantitative elasticity evaluation by contact resonance in an atomic force microscope.  
*Applied Physics A: Materials Science & Processing*, 66:S313–S317, 1998.



## C. Acknowledgements

At the beginning of this last chapter I would like to express my gratitude to **Prof. Dr. Stefan Weber**, who invited me in his group at the Max-Planck-Institute in Mainz and awakened my interest for the ferroelastic twin domains. He was a great supervisor, who always had an open door for me and took his time, when I had problems during my experiments. Furthermore, he gave me the opportunity to do measurements in the USA, which was a very enriching experience for me.

Thank you Stefan, I really appreciate your effort and wish you great fortune for the years to come!

As important as a good supervisor and an exciting topic is the working group environment, which accompanies oneself the whole time. For this matter, the **AK Butt** was a very good choice, especially the **Weberknechts** around Stefan with our enriching group meetings every week. Thank you guys for your cooperative and helpful behavior, this should not be taken for granted, especially when going to different sectors than natural sciences.

Special thanks to **Ilka Hermes**, who worked on this project before and introduced me patiently to the art of atomic force microscopy and dealing with certain chemicals, without poisoning myself. **Alexander Klasen** also helped me with parts of my sample preparation, e.g. the usage of the historically valuable gold evaporator and the plasma cleaner (certainly without to “destroy everything”). At this point, I also want to thank **Gabi Herrmann** for helping me with the  $\text{SiO}_2$  deposition on my substrates and her general helpfulness.

**Amelie Axt** spent some of her time to give small private lectures about Kelvin Probe Force Microscopy, the royal discipline among the AFM methods. Even if there was not quite enough time for me to master this method and get meaningful results for my thesis, I appreciate the gesture and thank her very much for that.

**Christopher Gort** started his studies in physics at the same time as I did and has been in the AK Weber since his Bachelor thesis. When working in the lab, he showed me some tricks for the AFM, which he was already familiar with when I just started my work. I am really grateful for this.

## C. Acknowledgements

---

Concerning my trip to the USA, I would like to thank **Liam Collins** and the people from the Oak Ridge National Laboratory in Tennessee for giving me the opportunity to spend some time there. Liam helped me with the organization before the visit and was very supportive with my measurements when I arrived. He even offered me a place to stay at his house and invited me to his family on the weekend. In the end, it was a good experience and I left the country with many great impressions.

In advance, I thank **Prof. Dr. Hans-Joachim Elmers** for taking his time to be the second referee for my thesis.

In my personal opinion, the enthusiasm for science can always be traced back to having good teachers in school, who give their best to transmit the spirit to their students. In this context, my gratitude goes to my former advanced course teachers in physics and mathematics, namely **Dr. Bernd Fischer** and **Gilles Lorenz**. Thank you for sharing your curiosity with me!

Without my friends, that I made over the years while sitting next to them in lecture halls, I would never have accomplished my studies in physics. Thank you guys for being there and sharing precious moments with me, that I will never forget. Now my time in Mainz has come to an end and soon, we will all go our separate ways into the future. I take those good memories with me and wish you all the best!

My enchanting girlfriend **Anja Winterling** 🐾 is one bright spot for my new life stage. Thanks to her encouraging motivational cards that she sent to me the last couple of weeks, I kept my motivation to finish my thesis in time. I appreciate her tolerance and patience, even when the time I spent on this thesis sometimes came at costs of our weekends. With her reminding me of the positive aspects of a new beginning, I am looking forward to my upcoming challenges.

Finally I would like to thank my family **Larissa**, **Mirella** and **Gunter Winkelmann** for always supporting me in good and bad times of my life. It is good to know, that there is a place, where I am always welcome and where people are waiting for me with open arms.